Wave-like motions and torques in Earth's core as inferred from geomagnetic data: a synthetic study

Tobias Schwaiger, Nicolas Gillet, Dominique Jault, Mathieu Istas, Mioara Mandea

Highlights

Wave-like motions and torques in Earth's core as inferred from geomagnetic data: a synthetic study

T. Schwaiger, N. Gillet, D. Jault, M. Istas, M. Mandea

- Torsional Alfven waves and quasi-geostrophic magneto-Coriolis waves are recovered from simulated geomagnetic data.
- The ability to recover transient flows depends on their magnitude, geometry and period, plus the data coverage and accuracy.
- Extrapolating throughout the core the inverted zonal surface flows, we predict well the core angular momentum changes.
- The core-mantle electromagnetic torque mainly arises from the axial rotation part of the core surface motion.
- The electrical currents, part of the dynamo process, leaking from the core interior yield a negligible torque on the mantle.

Wave-like motions and torques in Earth's core as inferred from geomagnetic data: a synthetic study

T. Schwaiger[a,b], N. Gillet[a], D. Jault[a], M. Istas[a], M. Mandea[b]

[a] *Univ. Grenoble Alpes, Univ. Savoie Mont Blanc, CNRS, IRD, Univ. Gustave Eiffel, ISTerre, Grenoble, 38000, France*
[b] *Centre National d'Etudes Spatiales, 2 place Maurice Quentin, Paris Cedex 01, 75039, France*

Abstract

Here, we present a synthetic validation for the inversion of transient fluid motions at the surface of Earth's core. It is based on a numerical simulation of the geodynamo in which the main time-scales (based on rotation, magnetic field and velocity) are sufficiently separated to give rise to a variety of hydro-magnetic waves. We focus the study on wave-like motions with periods commensurate to the Alfvén time, which is based on the strength of the magnetic field in the core interior. Synthetic magnetic data are generated over 90 Alfvén times, representative of the era covered by observatory and satellite measurements. These synthetic data are inverted to estimate a magnetic field model. Thereafter, we apply the `pygeodyn` data assimilation tool to recover core surface flows. We investigate the quality of their reconstruction as a function of their time scale. The success of the reconstruction depends on the data accuracy and coverage and on the magnitude of the flow. We also retrieve axi-symmetric torsional Alfvén waves, despite their relatively weak magnitude.

We use the synthetic data to investigate the exchanges of angular momentum between core and mantle that induce length-of-day (LOD) changes. These exchanges result from the electromagnetic torque between the fluid core and the mantle and the gravitational torque between the inner core and the mantle. The inverted flows convincingly predict LOD variations in the dynamo calculation. We find that core surface zonal motions match well with the geostrophic (axially invariant) motions at the origin of the LOD changes, on all considered time-scales. We also investigate the different contributions to the electro-magnetic torque. In the dynamo simulation, only a small part can be attributed to the leakage torque caused by electrical currents flowing from the core to

the mantle. The relative contribution from the poloidal field induced in the mantle, which amounts to about 1/3 of the total torque, is significantly larger than estimated in previous studies, based on geomagnetic observations. The remaining torque, which is associated with the toroidal induced field, mostly stems from the solid body rotation interacting with the radial magnetic field up to spherical harmonic degree 30.

Keywords:
Earth's core, Geomagnetic secular variation, Inverse problem, hydromagnetic waves, electro-magnetic torque, length-of-day

1. Introduction

The magnetic field **B** originating from the Earth's outer liquid core exhibits temporal variations over periods ranging from about one year to tens of millions of years. The first time derivative of the geomagnetic field, also referred to as the secular variation (SV), is often considered to represent the temporal evolution of the Earth's core magnetic field. Abrupt changes in the SV, the so-called geomagnetic jerks, are the most rapid features detected in time-series of the main magnetic field, involving time-scales from several months to a few years. They show up in magnetic records as sudden V-shaped changes of the SV, corresponding to a discontinuity in the second time derivative of the geomagnetic field (the secular acceleration, SA), or equivalently a Dirac-delta function in the third time derivative (Mandea et al., 2010). Continuous records of the three components of the geomagnetic vector field have only been available since Gauss established the first geomagnetic observatory in the middle of the 19th century (see Garland, 1979). Ancient magnetic field orientation measurements obtained mainly from navigation catalogs, provide direct observational constraints as far back as the late XVIth century (Jackson et al., 2000; Jonkers et al., 2003). This restricts the longest directly accessible periods to centennial time-scales (e.g., Matzka et al., 2010). These ground observations have been complemented by measurements from space provided by several satellite missions, occurring at irregular intervals in the second half of the 20th century and continuous during the last two decades (Lesur et al., 2022). In particular, data from CHAMP (2000–2010) and Swarm (2013–) satellite missions are crucial for accessing global rapid variations of the geomagnetic field down to periods of about one year (Hammer et al., 2021b; Baeren-

zung et al., 2022). Access to shorter time-scales is challenging because the core signal amplitude steeply decreases with increasing frequencies (Lesur et al., 2018). Hence, it is hidden by variations from magnetic field sources external to the Earth (magnetospheric and ionospheric fields, see Finlay et al., 2017). In addition, the weakly electrically conducting mantle acts as a low-pass filter and makes it impossible to observe changes in the core field on periods shorter than a few months (Jault, 2015).

The idea that temporal variations in the geomagnetic field could be the result of hydro-magnetic waves in the Earth's liquid outer core was first investigated by Hide (1966), Braginsky (1967) and Malkus (1967). Waves in the core may be coupled to the mantle and trigger fluctuations in its rotation rate, and thus in the length-of-day (LOD). On the basis of this rationale, Braginsky (1970) suggested that an apparent 60-year periodicity found in variations of the LOD could be explained by torsional Alvén waves, commonly also referred to as torsional oscillations. The restoring force for these waves is the magnetic tension between geostrophic cylinders (cylindrical surfaces of fluid whose axis is aligned with the Earth's rotation vector $\mathbf{\Omega}$). They consist of oscillatory motions of these cylinders that propagate in the direction perpendicular to $\mathbf{\Omega}$, at a speed $V_A(s) \propto \tilde{B}_s$ the r.m.s. (root mean square) of the cylindrical radial component of the magnetic field averaged over geostrophic cylinders (see e.g., Jault, 2003; Finlay et al., 2010).

The geostrophic nature of torsional oscillations allows us to infer them from the core surface flow. Core surface motions are estimated by inverting the radial induction equation that couples the SV of the geomagnetic field at the Core-Mantle Boundary (CMB) and the velocity field at the top of the core (Roberts and Scott, 1965). This inverse problem is highly non-unique since not all possible flows produce changes in the magnetic field (Backus, 1968). This velocity ambiguity is usually mitigated either by making assumptions about the core (surface) dynamics, the most common of which are that the flow is steady, purely toroidal, tangentially geostrophic or quasi-geostrophic (for a review, see Finlay et al., 2010; Holme, 2015), or by incorporating statistics derived from numerical geodynamo simulations as prior information (e.g., Fournier et al., 2011; Aubert, 2014; Barrois et al., 2017; Gillet et al., 2019).

The changes in core angular momentum carried by geostrophic motions, as estimated

from core surface velocities, do balance the changes in mantle angular momentum inferred from LOD data for periods ranging from $\approx$ 5 to 60 years (Jault et al., 1988; Jackson et al., 1993; Baerenzung et al., 2018; Gillet et al., 2019; Istas et al., 2023). The transfer of angular momentum between the core and the mantle is necessarily mediated by one or several torques, such as the electro-magnetic (EM), gravitational, pressure or possibly the viscous torque (Buffett, 1996; Jault, 2003; Roberts and Aurnou, 2012).

Isolating torsional waves in core surface flow models is a way to probe the magnetic field deep in the conducting core, otherwise inaccessible from magnetic observations alone. The LOD signal is stronger towards long periods (20-60 years), as is the case for the core surface flows. Torsional waves were therefore initially sought on decadal periods, for which LOD changes are of the order of 1 ms. Within this framework, the interpretation of magnetically inferred core surface motions implied that the field strength deep in the core should be of the order of a fraction of a mT (Zatman and Bloxham, 1997, 1999; Buffett et al., 2009). This estimate is less than the magnitude of the radial magnetic field downward continued from the Earth's surface to the core surface. It is at odds with numerical geodynamo simulations that favor a field about 10 times larger in the bulk of the core (Aubert et al., 2009) as well as with geophysical inferences of the field at the inner core boundary from nutation studies (Buffett et al., 2002; Koot et al., 2010). By estimating core flow models from magnetic data, Gillet et al. (2010) discovered outward propagating torsional waves of period 6-yr, implying a field intensity deep in the core of several mT, much larger than the radial field intensity at the core surface, as found in numerical geodynamo models. These waves explain a 6 yr oscillation in the LOD, of amplitude $\sim$ 0.15 ms, first detected by Abarca del Rio et al. (2000) – see Duan and Huang (2020) or Rosat and Gillet (2023) for more recent analyses.

The amplitude of the detected torsional waves (a fraction of km/yr) generate a SV signal at the Earth's surface of at most 2 nT/yr (Cox et al., 2016). This is too weak to explain the entirety of the magnetic signal observed on interannual time-scales, of the order of 10 nT/yr at the Earth's surface (the latter is itself small in comparison with the SV signal $\sim$ 100 nT/yr on the century time scale). Satellite data have indeed revealed oscillatory magnetic patterns that produce peaks in the norm of the SA roughly every three years (see Chulliat and Maus, 2014; Finlay et al., 2016). Downward continued at

the surface of the core, this interannual magnetic signal is the strongest in the equatorial belt (see Fig. 1 in Gillet et al., 2022a). Intense non-zonal interannual motions of several km/yr amplitude are required to explain these patterns (Gillet et al., 2015; Finlay et al., 2016; Kloss and Finlay, 2019). Such flow motions have since been interpreted as slow magneto-Coriolis (MC) waves (Gillet et al., 2022b), for which both the Lorentz and Coriolis forces participate to the restoring action. They have been assumed to be well approximated as quasi-geostrophic (QG) motions, meaning that the projection of the flow in the equatorial plane is invariant along $\mathbf{\Omega}$.

In the presence of a magnetic field, and for a fast enough global rotation, the frequency spectrum of hydromagnetic MC waves splits into two branches (Malkus, 1967): waves with periods longer than the Alfvén time are mainly magnetic, while waves with shorter periods are predominantly kinetic and consist of inertial waves only weakly affected by the magnetic field. This description also holds for QG motions, as put forward by Hide (1966). For the parameters of the Earth's core, and small wavenumbers, slow (resp. fast) MC waves have periods of centuries to millenia (resp. days to months) (e.g. Finlay, 2008). However, these waves are dispersive, and there exist slow QG MC waves with periods comparable to that of Alfvén waves ($\sim 5-10$ years), as first described numerically by Gerick et al. (2021). These are characterized by small length-scales in the cylindrical radial direction and low azimuthal wave number. Their identification is easier around the equator where small length-scales in the cylindrical direction correspond to medium length-scales in the meridional direction. Therefore, contrary to what has long been assumed, there are interannual QG MC waves detectable at the core surface (Gillet et al., 2022b).

The above interpretation is supported by numerical dynamo simulations run at parameters approaching Earth's conditions. Torsional waves have been detected in early dynamo simulations (Wicht and Christensen, 2010; Teed et al., 2014). They become ubiquitous as the simulation parameters take values closer to their geophysical estimates (Schaeffer et al., 2017; Aubert, 2018). However, it is only in simulations where the inertial, magnetic and convective time-scales are well separated that non-zonal QG hydromagnetic waves have been detected. This requires lowering the relative importance of viscous forces with respect to Coriolis forces, at the expense of a high numerical cost. In these

numerical geodynamos, geomagnetic jerks (i.e. events of enhanced magnetic acceleration) were first interpreted as the result of QG Alfvén waves, for which Earth's rotation dictates the geometry of the flow but plays no role in the restoring force (Aubert and Finlay, 2019). These transient responses, where inertia balances the magnetic force, tend to be regularly excited as the input parameters of the simulations are pushed further towards their geophysical estimates (Aubert and Gillet, 2021). They constitute the response of the fluid to disruptions to the long time-scale balance where at first order the pressure gradient equilibrates the Coriolis forces (quasi-geostrophy), followed by a balance between Magnetic, Archimedes and ageostrophic Coriolis forces (so called QG-MAC, see Schwaiger et al., 2019; Aubert, 2020). However, once scaled to geophysical units, QG Alfvén waves tend to present too short length-scales, at the limit of detection. Gillet et al. (2022b) discriminated QG Alfvén waves and QG MC waves from a discussion of their dispersion relation. Aubert et al. (2022) have since observed in their simulations that QG Alfvén waves triggered deep in the core (for instance by convective plumes) morph into QG MC waves while propagating outward. They also document shallower events, generated by plumes reaching intense magnetic field areas near the core surface. These provoke transient departure from the QG-MAC balance: a rapidly varying Lorentz force yields changes in the magnetic field configuration and emission of QG hydro-magnetic waves in a region where there are gradients in $\mathbf{B}$ to ensure matching of the magnetic field with a potential field. According to this scenario, geomagnetic jerks observed at the Earth's surface are concomitant with the propagation of waves similar to either QG Alfvén or QG MC waves according to their location in the core interior. The events that are labelled as jerks in geophysical records are mostly related to QG MC waves, because of their relatively longer length and/or time-scales.

Numerical dynamos have long been used as a testing ground for core flow imaging methods. First attempts have dealt with instantaneous estimates of the secular variation and of the flow (Rau et al., 2000; Amit et al., 2007; Fournier et al., 2011; Aubert, 2013). These works have paved the way for time-dependent core surface flow imaging tools that rely on prior information (mean and covariances) built from dynamo simulations (Barrois et al., 2017; Gillet et al., 2019; Sanchez et al., 2019). Here, we use a numerical dynamo to investigate the detectability of hydromagnetic waves instead of instantaneous flows as

before. For this purpose, we design a synthetic set-up from a free geodynamo run, namely the '*71p*' dynamo (Aubert and Gillet, 2021), in which the outer core and the mantle are coupled directly via an electromagnetic torque due to a conducting layer at the base of the mantle, and indirectly via a gravitational torque between the inner core and density anomalies in the mantle. Our investigation is kept as close as possible to the geophysical configuration, in order to assess from which epoch geomagnetic data are accurate enough to detect waves in the core. Therefore, in order to reflect the time variable accuracy of geomagnetic measurements, we generate synthetic magnetic records from the dynamo simulation with the same sites and time distribution as the data set used to build the COV-OBS-x2 model (Huder et al., 2020). Then, we test the core surface flow imaging tool `pygeodyn` (Huder et al., 2019) with magnetic field models built from this synthetic data set. Focusing on time changes of the surface flow led us to consider also time series of the torques responsible for changes in the mantle angular momentum (and thus of the LOD).

This paper is organized as follows. In Section 2 we first describe how we design the synthetic setup (from the dynamo synthetic data to the core flow inversion). Section 3 shows how well we recover both zonal and non-zonal interannual and decadal flows. Protocols used to estimate the core angular momentum changes and the core-mantle electromagnetic torque are evaluated in Sections 4 and 5. Finally, Section 6 focuses on the geophysical implications of our study.

2. Data and Method

2.1. Dynamo data from numerical simulations

For numerical geodynamo simulations to realistically reflect the richness of the dynamics expected in the Earth's outer core, it is required that several ratios between characteristic time-scales are of the correct order of magnitude. The most relevant time-scales are

- the inverse of the planetary rotation rate $\tau_\Omega = 1/\Omega$, with $\Omega \simeq 7.3 \times 10^{-5}$ s^{-1},
- the Alfvén time $\tau_A = d/U_A \approx 2$ yr, with $d = 2265$ km the radial distance between the inner and outer core boundaries of radii $r_i = 1220$ km and $c = 3485$ km

and $U_A = B/\sqrt{\rho\mu} \sim 1000$ km/yr the Alfvén speed, using $B \sim 4$ mT the typical magnetic field intensity inside the core (Gillet et al., 2010), $\rho \simeq 10^4$ kg/m^3 the outer core density and $\mu = 4\pi \times 10^{-7}$ H/m its magnetic permeability,

- the convective overturn time $\tau_U = d/U \approx 150$ yr, with $U \sim 15$ km/yr a characteristic amplitude for the large scale fluid velocity (e.g., Finlay et al., 2010),
- the magnetic diffusion time $\tau_\eta = d^2/\eta \approx 150$ kyr, with $\eta \sim 1$ m^2/s the magnetic diffusivity of the liquid iron core (e.g., Pozzo et al., 2012),
- the viscous diffusion time $\tau_\nu = d^2/\nu \approx 150$ Gyr, with $\nu \sim 10^{-6}$ m^2/s the kinematic viscosity (de Wijs et al., 1998). From this time, we derive the Ekman spin up time (Greenspan, 1968), $\tau_{Ek} = (\tau_\nu/\Omega)^{1/2} \approx 10^4$ years, characteristic of the fluid response driven by Ekman suction to any differential angular velocity between the fluid and the solid boundaries. It measures the importance of the viscous torque at the core surface.

In the Earth's core, the above time-scales rank as follows (e.g., Gillet et al., 2022a):

$$\tau_\Omega \ll \tau_A \ll \tau_U \ll \tau_{Ek} \ll \tau_\eta \ll \tau_\nu. \tag{1}$$

The dynamical regime of the outer core can be characterized in terms of ratios between these time-scales. The most commonly considered ones are the Ekman number $E = \tau_\Omega/\tau_\nu = \nu/\Omega d^2 \sim 10^{-15}$, the magnetic Reynolds number $R_m = \tau_\eta/\tau_U = Ud/\eta \sim 10^3$ (diffusion is slower than advection on large length-scales), and the magnetic Prandtl number $P_m = \tau_\eta/\tau_\nu = \nu/\eta \sim 10^{-6}$ (momentum diffuses much less rapidly than magnetic perturbations). Of particular interest for understanding the rapid dynamics is also the Alfvén number $Al = \tau_A/\tau_U = U/U_A \sim 10^{-2}$ (Alfvén waves travel much faster than the fluid velocity).

For simulations of the Earth's dynamo, the correct relationship between the magnetic diffusion time and the convective overturn time (Christensen et al., 2010), which defines the magnetic Reynolds number R_m, is of central importance. While Earth-like values of R_m can be readily achieved, separating τ_U and τ_A by two orders of magnitude has proven difficult in the direct numerical simulations due to computational limitations (e.g., Schaeffer et al., 2017). We rely here on the computation by Aubert and Gillet (2021). It

belongs to the family of 'path dynamos', which sets a trajectory in the parameter space (E, P_m) as a function of a single parameter ϵ. In this framework the distinguished limit $\epsilon \to 0$ would correspond to geophysical dynamos (Dormy, 2016). Along the path, the thermochemical forcing is increased as $\epsilon \to 0$, while the magnetic field morphology is preserved. A wide range of spatial and temporal scales have to be resolved numerically because E and P_m are lowered simultaneously. The simulation by Aubert and Gillet (2021) (so-called *71p* model) involves hyperdiffusion for the small length-scales (spherical harmonic degrees $n > 30$) of the fluid flow and co-density fields (Aubert et al., 2017).

Path dynamos are run with stress-free boundary conditions. In this configuration, τ_{Ek} is meaningless since there is no viscous torque on either of the two boundaries. In the *71p* simulation considered here, the temporal evolution of the core angular momentum is then entirely determined by

(i) the gravitational torque between the inner core and the mantle (in a scenario where mass anomalies in the mantle induce a non-spherical geopotential and consequently deformations of the inner core), and

(ii) the electro-magnetic torque acting on the conducting mantle (Pichon et al., 2016; Aubert et al., 2022).

Motions in the Earth's outer core are coupled to the inner core rotation. The gravitational torque in the path dynamos is considered in the limit where the viscous relaxation time τ_G of the inner core is short compared to the investigated time-scales. Therefore, any misalignment between the shape of the inner core and the gravity equipotential at $r = r_i$ is accommodated by viscous deformations on these time-scales. This comes down to neglecting inertia in the equation for the inner core angular momentum, excluding scenarii involving a possible resonant response of the inner core that may force geostrophic motions in the fluid core around a given period (e.g., Mound and Buffett, 2003, 2005). From the parameters of the simulation, the viscous relaxation time is $\tau_G \approx \tau_A/8$ (Aubert et al., 2022). Considering surface flows with time-scales $\tau \gg \tau_A/8$, we are consistent with the assumption of short viscous relaxation time used in the dynamo model. The τ_G value, inherited from the path dynamos (Aubert et al., 2013, 2017), has been set to favor a persistent westward drift of the core surface with respect to the mantle rather

than a long-term super-rotation of the inner core (see Pichon et al., 2016, Fig. 3).

The EM torque in the path dynamos is considered in the thin layer approximation, with the thickness Δ of the electrically conducting layer at the base of the mantle such that $\Delta \ll (\tau/\sigma_m\mu)^{1/2}$, in order to ensure continuity of the radial magnetic field across that layer. Here τ is the shortest investigated time-scale of the flow and σ_m is the electrical conductivity of the mantle. The conducting layer in the simulation has a conductance $G = \Delta\sigma_m = 10^{-4}d\sigma_c$, with $\sigma_c = 1/(\mu\eta)$ the electrical conductivity of the fluid outer core. The conductance in the dynamo simulation is in line with estimates ($G \sim 10^8$ S) from studies of the EM torque (Holme, 1998) and of torsional waves (Schaeffer and Jault, 2016).

In the following we use the shell thickness d as length unit and the Alfvén time τ_A as time unit. As a result, velocities are scaled based on the Alfvén speed $U_A = d/\tau_A$. We consider the spherical coordinate system (r, θ, ϕ) with unit vectors $(\mathbf{1}_r, \mathbf{1}_\theta, \mathbf{1}_\phi)$ in the radial, ortho-radial and azimuthal directions. We rely on time series of the Gauss coefficients (g_n^m, h_n^m) for the magnetic field at the core surface, described through the magnetic potential

$$V(r \geq c, \theta, \phi) = a \sum_n \left(\frac{a}{r}\right)^{n+1} \sum_m \left(g_n^m \cos m\phi + h_n^m \sin m\phi\right) P_n^m(\cos\theta)\,, \tag{2}$$

with P_n^m the Schmidt semi-normalized Legendre polynomials and $a = 6371$ km the Earth's reference radius. We also consider time-series of the spherical harmonic coefficients $({}^{c,s}t_n^m, {}^{c,s}s_n^m)$ for the horizontal flow at the top of the core. The latter are described via the toroidal (T) and poloidal (S) scalars as defined by Holme (2015):

$$\mathbf{u}_h = \nabla \times (Tr\mathbf{1}_r) + \nabla_h (rS)\ . \tag{3}$$

T and S are decomposed in spherical harmonics as

$$\left\{ \begin{array}{ll} S(\theta,\phi) = & \displaystyle\sum_n \sum_m \left({}^c s_n^m \cos m\phi + {}^s s_n^m \sin m\phi\right) P_n^m(\cos\theta) \\ T(\theta,\phi) = & \displaystyle\sum_n \sum_m \left({}^c t_n^m \cos m\phi + {}^s t_n^m \sin m\phi\right) P_n^m(\cos\theta) \end{array} \right. . \tag{4}$$

Data for the dynamo model used as reference (from which synthetic data are generated, see Section 2.2) are provided by the *71p* numerical geodynamo simulation. It was run for parameters $(E, P_m) = (3\times10^{-10}, 7.9\times10^{-3})$, and yields $(R_m, Al) \approx (1100, 0.049)$.

The period considered here spans the time interval $[8500, 9022]$, in time units of years (as initially scaled by the authors) and covers one geomagnetic jerk, as described by Aubert et al. (2022). The model data are freely available at `https://4d-earth-swarm.univ-grenoble-alpes.fr/data`. Data considered to build the spatio-temporal prior used for the core-flow inversion (see Section 2.3) are extracted from the *50p* simulation obtained with the parameters $(E, P_m) = (10^{-8}, 4.5 \times 10^{-2})$ (Aubert et al., 2017). This calculation yields a similar value of R_m as the *71p* simulation, because R_m is an invariant of the dynamo path. Data from the *50p* simulation covers a time-span of 20 000 yrs.

2.2. Synthetic geomagnetic field model

We generate a synthetic data set from the time-series of Gauss coefficients. It has the same spatio-temporal distribution as the data set used to build the COV-OBS-x2 models (Huder et al., 2020). On top of surveys and historical data, the bulk of the data stems from observatory and satellite observations. It is worth noting that the quality and quantity of observatory records improved significantly after 1960, with the advent of proton magnetometers and the efforts initiated during the International Geophysical Year in 1958. We consider observatory data as annual differences of annual means prior to 1997, and then annual differences of 4-monthly means. Observatory data provide continuous time series at fixed locations, with a coverage naturally biased towards continents. Conversely, low Earth orbiting satellites provide an almost global spatial coverage, with data along tracks. The temporal sampling of the core field by polar orbiting satellites is limited by their slow coverage of all local times (of the order of several months to a year, depending on the configuration). In the construction of the COV-OBS models, data from the CHAMP (2000–2010) and Swarm (2013–2020) missions are considered through geomagnetic virtual observatories (as initiated by Mandea and Olsen, 2006). The 4-month geomagnetic virtual observatories series consist of spatio-temporal regressions at fixed points in space (see Hammer et al., 2021a,b). Prior to the past two decades, several missions also brought valuable information: the POGO (1965–1970), DE-2 (1981–1982) series and MAGSAT (1979) satellites.

The COV-OBS-x2 model describes the time evolution of the magnetic field Gauss coefficients up to spherical harmonic degree 14, and covers 180 years from 1840 to 2020. To build the synthetic data set, years are transformed into Alfvén units: the synthetic

model thus spans 90 τ_A. Gaussian random noise, scaled according to the error variances of the geomagnetic datasets (see Gillet et al., 2013; Huder et al., 2020, and references therein), is added to the synthetic data output of the simulation. An ensemble of models is then inverted from these data with the same software as that used for the reconstruction from geomagnetic observations.

The COV-OBS models result from a stochastic inversion, where the a priori information added to reduce non-uniqueness issues is based on temporal cross-covariances compatible with the occurrence of geomagnetic jerks. They are indeed constructed upon correlation functions characteristic of second-order stochastic processes, for which the first time-derivative is continuous but not differentiable, as are magnetic series sampled every year or so (see Gillet et al., 2013). The a priori variances of the Gauss coefficients, independent of the order m (except for the axial dipole), are deduced from spatial magnetic spectra obtained over the satellite era. The model is composed of an ensemble mean, together with an a posteriori covariance matrix, which is used to estimate the uncertainty level on the Gauss coefficients and on their SV. These constitute entries for the sequential recovery of core flows with the `pygeodyn` data assimilation tool. The time resolution of the COV-OBS model is defined by the projection onto spline functions of order 4, with knots every 2 yrs (or 1 τ_A). This choice results from a compromise dictated by the use of data with highly variable accuracies. It implies a cut-off period on time-scales $\lesssim$ 4 yr= 2 τ_A (see Fig. 5a in Pick et al., 2019). A similar temporal projection has been applied when building the model from synthetic data, with knots every 1 τ_A.

2.3. Inverting for the simulated core surface flow

For the inversion of core surface motions, we rely on the `pygeodyn` software (Huder et al., 2019). It is based on an Ensemble Kalman filter (Evensen, 2003), a data assimilation algorithm composed of a succession of forecast (time integration of a forward model) and analysis (regression of the observations) steps. We consider here the trajectory of an ensemble of $N_e = 400$ realizations.

The evolution of the large scale radial field at the core surface is forecasted using the radial induction equation, once projected onto large length-scales (here denoted by

overlines):

$$\partial_t \overline{B}_r = -\overline{\nabla_h \cdot \left(\overline{\mathbf{u}}_h \overline{B}_r\right)} + e_r \,. \tag{5}$$

We thus also consider evolution equations for the large scale horizontal flow $\overline{\mathbf{u}}_h$ at the core surface, as well as for the errors of representativeness e_r. These latter account for magnetic diffusion at the top of the core, and more importantly for the projection onto large length-scales of the induction processes involving unmodeled small scale velocity and magnetic fields (Gillet et al., 2019). All fields are projected onto spherical harmonics, with truncation levels respectively $n_b = 13$ for $\overline{B}_r$ and e_r and $n_u = 18$ for $\overline{\mathbf{u}}_h$. These three fields (radial field, flow, error term) constitute the 'augmented' model state. The evolution for $\overline{\mathbf{u}}_h$ and e_r is governed by multivariate stochastic equations, whose parameters are anchored to spatio-temporal statistics extracted from the *50p* dynamo simulation, as described in Gillet et al. (2019). In particular, in order to build the operators entering the stochastic models for $\overline{\mathbf{u}}_h$ and e_r, the dynamo is sampled every $\Delta t^* = 0.862\tau_A$. The integration of the forward model – stochastic equations as well as equation (5) – is operated with a forecast time-step $\Delta t^f = 0.129\tau_A$, while analyses are operated every $\Delta t^a = 2\Delta t^f$.

At each analysis step, we first perform a regression of the main field Gauss coefficient data (provided for $n \leq n_b$), to get a sample of N_e analyzed large scale fields $\overline{B}_r$. With this knowledge, an analysis of the SV Gauss coefficient data (for $n \leq n_b$) is then performed to invert for an ensemble of N_e realisations for $\overline{\mathbf{u}}_h$ and e_r. Gauss coefficients (main field and SV) data, together with their uncertainties, are provided by the synthetic field model as detailed in Section 2.2. At each analysis step, the Kalman gain matrix requires the computation of the forecast state cross-covariance matrix, first for the coefficients describing $\overline{B}_r$, then for those of $\overline{\mathbf{u}}_h$ and e_r together. It is built from the ensemble of N_e realizations of the forecast core state. This ensemble being of finite size, a crude estimate of these second order statistics will be noisy, which can lead for instance to ensemble collapse (i.e. unrealistic decrease of the ensemble spread). We thus follow Istas et al. (2023), and use the 'Graphical Lasso' method (e.g., Friedman et al., 2007), which mitigates the impact of noise, while keeping as much as possible the information contained in the empirical cross-covariances. This method involves a tuning parameter that controls the sparsity of the forecast covariance matrices. It is chosen in a manner

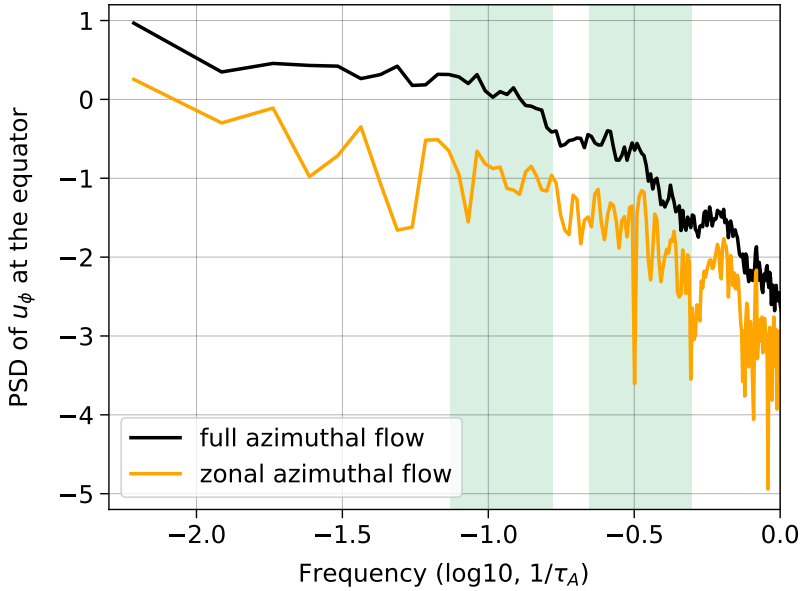

Figure 1: PSD for the azimuthal flow $u_\phi(\pi/2, \phi)$ at the core equator, for the total flow (black) and its zonal mean (orange). The PSD has been averaged over all longitudes. Frequency ranges considered for the analysis of band-pass solutions are also shown (green).

similar to that proposed by Istas et al., based on a likelihood criterion.

3. Recovery of transient core surface motions

3.1. Statistical analysis to assess the quality of the recovery

Analysis of core surface motions in the dynamo simulation investigated here has previously revealed enhanced energy in a variety of frequency ranges, at periods longer than τ_A (see Fig. 9c in Gillet et al., 2022a), more intense in the equatorial belt. As the purpose of the present study is to evaluate our ability to properly recover transient core surface flows from magnetic records, we focus on two period bands where oscillations have been isolated: $[6 - 13.5]\,\tau_A$ and $[2 - 4.5]\,\tau_A$, centered on respectively $T_0 = 3$ and 9 yr periods, with a bandwidth $\Delta T = 1.2T_0$ (see Fig. 1). We apply a band-pass filter to the flow in order to isolate rapid fluctuations, because the core surface motions present a red spectrum: the longer the period, the stronger the flow magnitude, as expected from

the SV spectrum (see for instance discussions in Gillet et al., 2015; Lesur et al., 2018; Aubert and Gillet, 2021). We use a causal Butterworth filter of order 2.

Let us introduce our diagnostics. The notation $x^\dagger = \frac{1}{N_e}\sum_{k=1}^{N_e} x_k$ stands for the average over the ensemble of realizations $\{x_k\}_{k\in[1,N_e]}$ for any inverted (or analyzed) quantity x^a. We also write $\tilde{x}(t)$ to represent a quantity $x(t)$ once band-pass filtered, while a quantity x from the reference dynamo fields is referred to as x^*. In the following, we focus on the azimuthal flow component u_ϕ, for which the signal is the strongest (see Gillet et al., 2022b). In order to assess the quality of the filtered flow recovery at a specific longitude ϕ_0, we rely (on top of visual inspection) on two diagnostics: the correlation coefficient

$$c(t,\phi_0) = \frac{\left\langle \left\langle \tilde{u}_\phi^*(\theta,\phi_0,t)\tilde{u}_\phi^\dagger(\theta,\phi_0,t)\right\rangle_\theta\right\rangle_T}{\sqrt{\left\langle \left\langle \tilde{u}_\phi^*(\theta,\phi_0,t)^2\right\rangle_\theta\right\rangle_T \left\langle \left\langle \tilde{u}_\phi^\dagger(\theta,\phi_0,t)^2\right\rangle_\theta\right\rangle_T}}\,, \tag{6}$$

and the normalized misfit

$$m(t,\phi_0) = \frac{\left\langle \left\langle \left|\tilde{u}_\phi^*(\theta,\phi_0,t) - \tilde{u}_\phi^\dagger(\theta,\phi_0,t)\right|\right\rangle_\theta\right\rangle_T}{\left\langle \left\langle \left|\tilde{u}_\phi^*(\theta,\phi_0,t)\right|\right\rangle_\theta\right\rangle_T}\,, \tag{7}$$

where the sliding time average over $2T$ and the latitudinal average are respectively

$$\langle f(t)\rangle_T = \frac{1}{2T}\int_{t-T}^{t+T} f(t)\,\mathrm{d}t \quad\text{and}\quad \langle f(\theta)\rangle_\theta = \frac{1}{2}\int_0^\pi f(\theta)\sin\theta\,\mathrm{d}\theta\,. \tag{8}$$

We calculate the misfit and correlation coefficients using $T = 1.5\,T_0$, i.e. averaging over a duration slightly longer than the upper cut-off period of the filter – reducing this way short period oscillations in diagnostics series. When focusing on the azimuthal (or zonal) average instead of a specific longitude, we consider the quantities $c_z(t)$ and $m_z(t)$, obtained with equations similar to (6–7), replacing $\tilde{u}_\phi(\theta,\phi_0,t)$ by $\tilde{u}_\phi^0(\theta,t) = \frac{1}{2\pi}\int_0^{2\pi}\tilde{u}_\phi(\theta,\phi,t)d\phi$.

We conduct tests to evaluate the relevance of these diagnostics and define significance thresholds. We consider 10 azimuthal velocity time series of the *7i1p* dynamo, starting every $100\tau_A$ (each $90\tau_A$ long, in order to avoid over-lapping), and band-pass filtered between 6 and 13.5 τ_A. We furthermore consider 10 such series from the reduced stochastic model embedded into the `pygeodyn` assimilation tool, and anchored to the dynamo spatio-temporal statistics (see Gillet et al., 2019). For each pair built from those

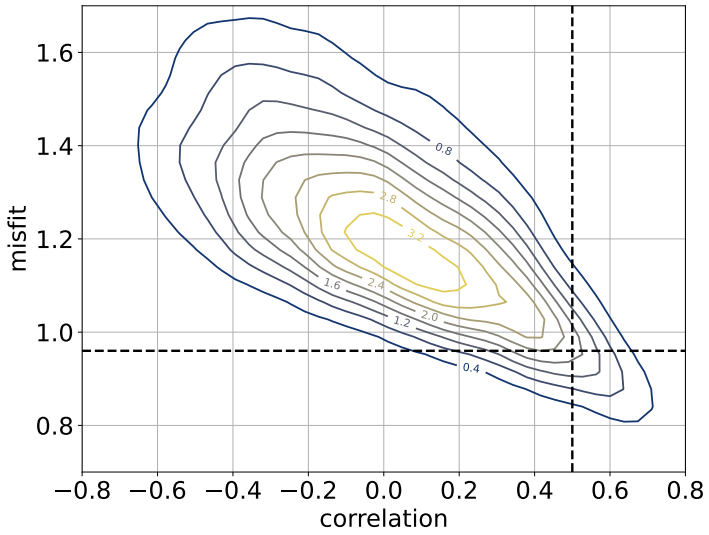

Figure 2: Probability distribution in the plane (c, m), obtained from all possible combinations between 10 decorrelated samples of the *71p* dynamo and 10 decorrelated samples of the reduced stochastic model (see text for details).

two sets, we calculate the misfit and correlation at 9 azimuths ϕ_0 regularly spanning $[0, 2\pi]$. The probability distribution in the plane (c, m) obtained from these samples is shown in Fig. 2. It turns out that the two diagnostics are tightly related, and that a low misfit is observed almost exclusively when the correlation is high. Misfits are in average higher than 1, because the diagnostics m involves the difference of two series, which amplitude is larger than that of each of the two series when they are decorrelated. A correlation $c > 0.5$ has been found in only $\approx 5\%$ of the occurrences. Sorting the samples by increasing misfits indicates that the 'best' 5% correspond to $m < 0.96$. Similar scores are observed when calculating the correlation and misfit between two decorrelated series from the dynamo. The scores are found to vary little with the period range considered for the band-pass filtering. They do not change much either when focusing on the zonal motions. The threshold of 5% for the criteria $c > 0.5$ and $m < 0.96$ is used in the following to assess the robustness of the transient flow inversion from synthetic magnetic data.

3.2. Flow recovery on periods $T \in [6 - 13.5]\,\tau_A$

We first analyze time-latitude diagrams for the flow band-pass filtered between 6 and 13.5 τ_A. We compare the filtered reference dynamo flow $\tilde{\mathbf{u}}_h^*$ to the ensemble average of the inverted filtered flow models $\tilde{\mathbf{u}}_h^\dagger$, for the two longitudes $\phi_0 = 90°$E and $\phi_0 = 10°$W (respectively in Fig. 3 and 4). These two longitudes appear representative of the simulation.

The dynamo displays wave-like patterns that are modulated in time and propagate preferentially equatorward. The flow amplitude is of the order of $U \approx U_A/50$. The strongest patterns in Fig. 3 around epoch $65\,\tau_A$ coincide with the jerk event #9, as documented by Aubert et al. (2022). Similar to flows inverted from geomagnetic observations, the fluid motions are the strongest next to the equator, and predominantly equatorially symmetric outside the tangent cylinder. The amplitude of the velocity patterns and their time evolution vary with longitude. A clear equatorward propagation is observed. Velocity fluctuations cross the core in a time of the order $15\,\tau_A$, i.e. they travel at a speed $C \approx U_A/15$ significantly larger than the typical velocity amplitude U.

After the epoch representative of the geophysical year ($t \gtrsim 60\tau_A$), the condition $c > 0.5$ and $m < 0.96$ is satisfied over most of the considered time-span, a much larger fraction than the 5% threshold from statistical tests. This renders unlikely a chance recovery of these transient core motions when a good enough network of observatories is available. This condition even slightly extends to $\approx 55\tau_A$ and $40\tau_A$ at respectively $\phi_0 = 90°$E and 10°W (see Fig. 3 and 4). Meanwhile, even during the satellite era, which spans approximately $[80, 90]\tau_A$, the conditions $c > 0.5$ and $m < 0.96$ are not always satisfied, depending on the longitude. Then, failure of a trustful recovery most often occur where and when the flow magnitude is weak.

Indeed motions are best recovered at epochs where the reference flow is the strongest, as seen in at 90°E over the period $[55 - 75]\,\tau_A$ (Fig. 3). At this longitude, the correlation at these epochs is up to ≈ 0.8, and the misfit down to about 0.75. The best diagnostics are not found during the era of nearly continuous satellite coverage. Meanwhile, at 10°W (Fig. 4), the correlation is clearly better starting from $t \simeq 55\,\tau_A$ (for which $c \gtrsim 0.7$), an era when the signal is significant even though less intense than at earlier stages. This signals the positive impact of an enhanced data constraint.

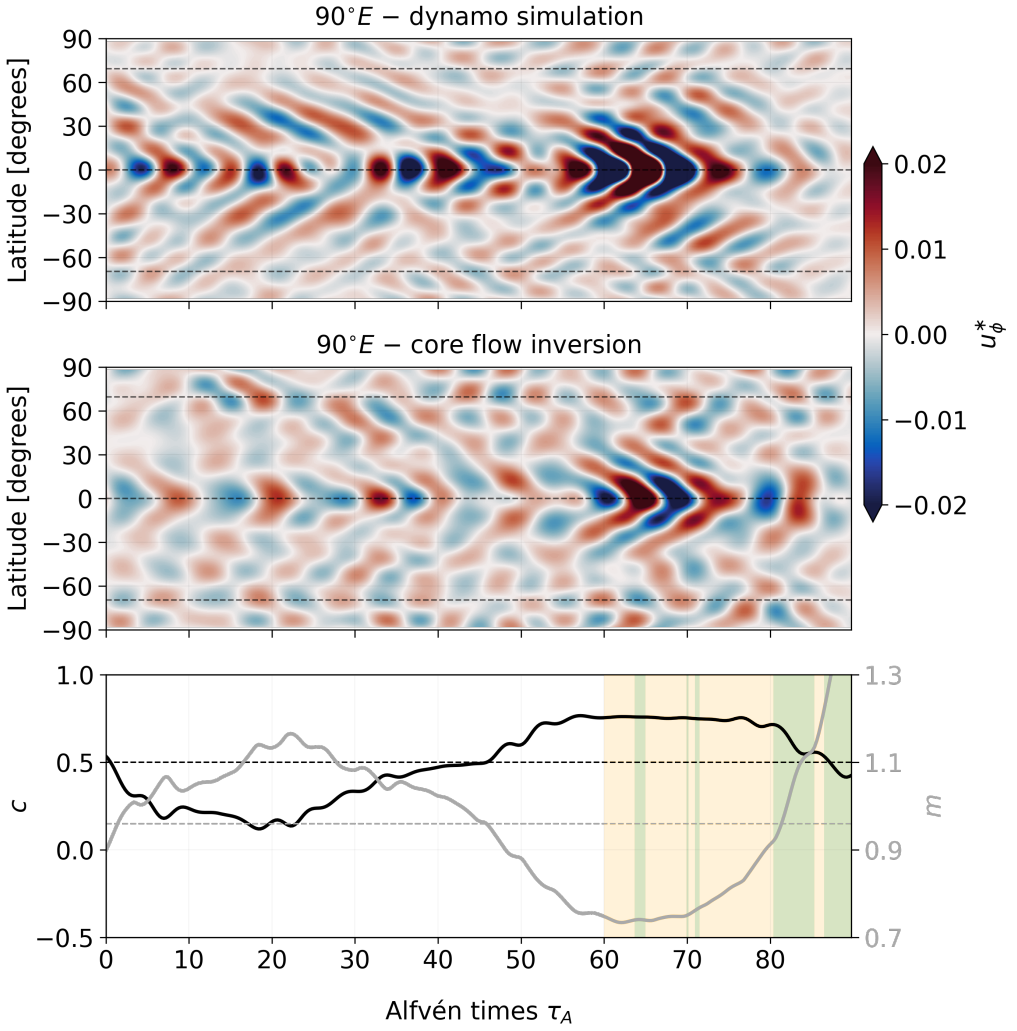

Figure 3: Time-latitude diagrams for the azimuthal flow band-pass filtered between 7 and 13 τ_A, at longitude $\phi_0 = 90°$E: reference dynamo flow (top) and ensemble average of the inverted flow models (middle). See text for details. The horizontal dashed lines (top and middle panels) correspond to the locations of the equator, and of the intersection between the tangent cylinder and the core surface. Bottom: correlation coefficient c (black) and misfit m (grey) – see Eq. (6) and (7). The dotted lines at $c = 0.5$ (black) and $m = 0.96$ (grey) correspond to the 5% of positive recovery threshold from the statistical test (see Section 3.1 for details). Shaded areas correspond to the times when satellite measurements are available (green) and to the era with the most numerous ground stations and the highest accuracy magnetometers (orange).

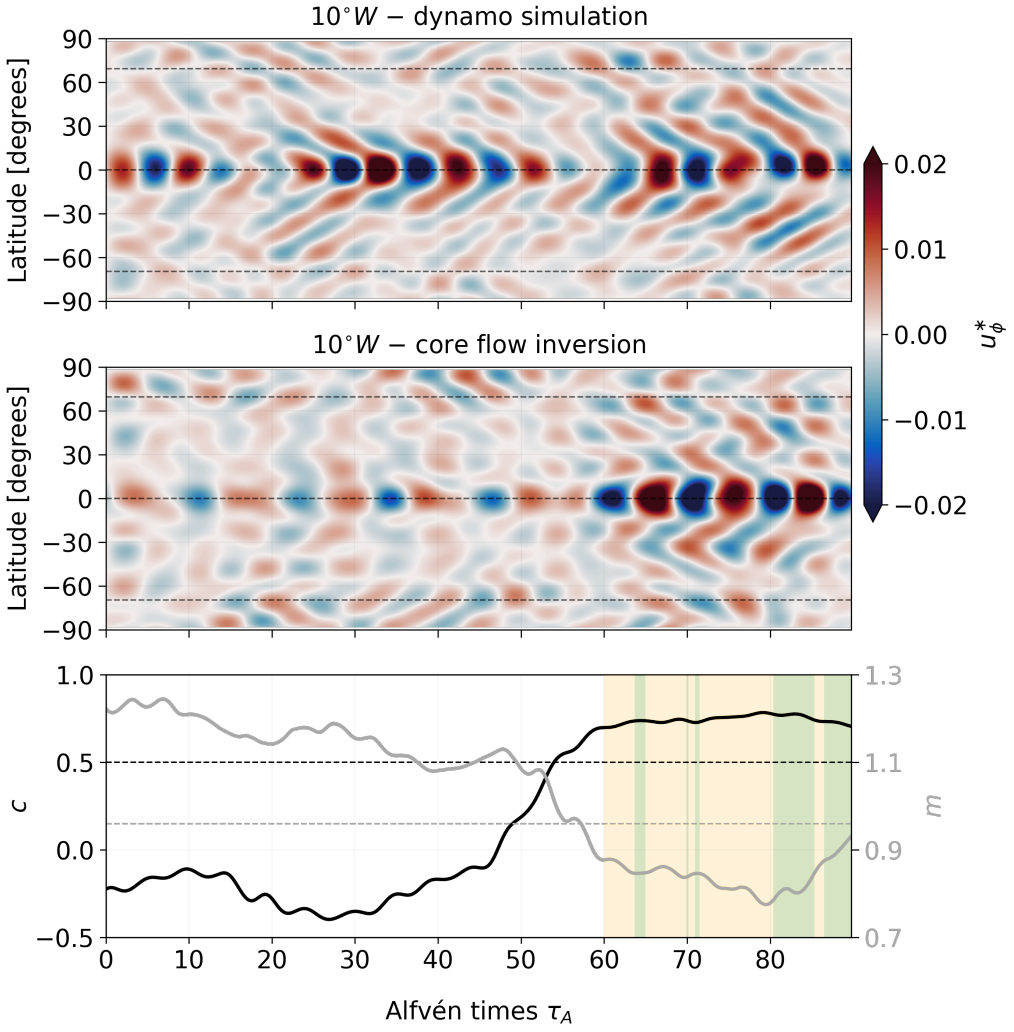

Figure 4: Same as Fig. 3, for longitude $\phi_0 = 10°$W.

Note that depending on the considered epoch and longitude, the outward propagation can be only partially rendered in the inverted flow, implying a wave speed sometimes under- or over-estimated from the inverted flow model. Nevertheless, flow patterns are overall convincingly recovered from the advent of modern measurements. The examples provided here illustrate how well we recover decadal wave-like patterns at the top of the core from geomagnetic field models: imperfectly, but still significant information can be extracted. It also gives a hint of the variety of behaviors that can be envisioned from the Earth's core dynamics over a duration of the order of one century.

3.3. Flow recovery on periods $T \in [2-4.5]\,\tau_A$

We now turn to the analysis of transient motions over shorter time-scales, by comparing the reference and inverted azimuthal flows band-pass filtered at periods within $[2-4.5]\,\tau_A$. In Fig. 5, we compare the filtered reference dynamo flow $\tilde{u}^*_\phi$ to the ensemble average of the inverted filtered flow models $\tilde{u}^\dagger_\phi$, for longitude $\phi_0 = 140°$E, while in Fig. 6 we focus on the retrieval of zonal motions.

The magnitude of the strongest non-zonal motions is of the order of $U \sim U_A/50$, similar to what we saw above in the lower frequency band. However, the strongest flow patterns appear here more confined to the equator, thus corresponding to a lower overall kinetic energy as expected from the SV temporal spectrum decreasing with frequency (see Fig. 1). The azimuthal flow patterns in this higher frequency range appear strongly modulated over timescales of the order of $10\,\tau_A$. They present obvious equatorward propagation, at a speed $C \approx U_A/10$ faster than the flow patterns investigated at periods $6-13.5\,\tau_A$. The propagation is particularly clear after $65\,\tau_A$, the epoch of the strong jerk #9 in the simulation (Aubert et al., 2022). Still, wave-like motions in the range $2-4.5\,\tau_A$ appear continuously excited.

The fraction of investigated time-span where the criteria $c > 0.5$ and $m < 0.96$ are satisfied amounts to about 30% of the era following the geophysical year better covered by ground-based stations ($t \gtrsim 60\tau_A$). It is thus significantly larger than the fraction (of the order of 5%) found from statistical tests although the corresponding fraction for longer time-scales is almost 100%. This indicates a better recovery towards lower frequencies.

The time-span when motions are recovered in the representative example of Fig.5 coincides with the strong transient motions and associated SV signal of jerk #9 in the

71p simulation. As it was also the case over longer periods, the quality of the core surface flow recovery is best when the azimuthal flow in the simulation is the strongest (see the higher correlation rate and the lower misfit for the time interval $58\tau_A \lesssim t \lesssim 72\,\tau_A$). The misfit values remain rather high ($m > 0.8$) because the magnitude is underestimated even when the phase is well captured (as witnessed when $c(t) \approx 0.7$). At epochs with rather poor coverage, when the flow is intense enough, part of the simulation flow may be recovered (see for instance the time interval $30 - 40\,\tau_A$, with c approaching 0.5 and m marginally above 0.96).

Let us now discuss the zonal motions (see Fig. 6). The first property to notice is their much weaker magnitude. This feature of dynamo flows, already documented by Aubert (2018) and Aubert and Gillet (2021), is also found in the analysis of flow models inverted from geomagnetic data (e.g., Gillet et al., 2015; Kloss and Finlay, 2019). Despite its weaker magnitude, it appears that the zonal flow can be more accurately recovered than the non-axisymmetric flow. Over the whole era after the geophysical year, c_z is continuously above 0.5 (around about 0.7) and m_z is below 0.96 (down to about 0.8), meaning that the recovery of zonal motions does not occur by chance, despite their weak amplitude and the short period considered. This is likely due to the simpler geometry of the zonal motions, which requires a lesser data constraint to be recovered. Even at earlier epochs ($t \in [25 - 37]\,\tau_A$, or around $45\tau_A$) the correlation coefficient is relatively high and some phases are correctly recovered, while the amplitude is under-estimated.

4. Core angular momentum changes predicted from core surface flows

4.1. Core angular momentum changes

By conservation of angular momentum of the whole Earth's system, time variations in the core axial angular momentum $L_z(t)$ produce opposite changes in the mantle angular momentum, and thus fluctuations $\Omega(t)$ in the Earth's rotation rate, i.e. in the LOD $2\pi/\Omega$. Taking the core density as uniform and neglecting the density jump at the inner core boundary, we obtain

$$\begin{aligned} L_z(t) = & \quad \mathbf{1}_z \cdot \int_{\mathcal{V}} \rho r \mathbf{1}_r \times (\mathbf{u} + r\Omega(t)\mathbf{1}_z \times \mathbf{1}_r)\, \mathrm{d}\mathcal{V} \\ = & \quad I_c \Omega(t) + 2\pi\rho \int_0^c \int_0^\pi r^3 u_\phi^0(r,\theta,t) \sin^2\theta \mathrm{d}r\mathrm{d}\theta\,. \end{aligned} \tag{9}$$

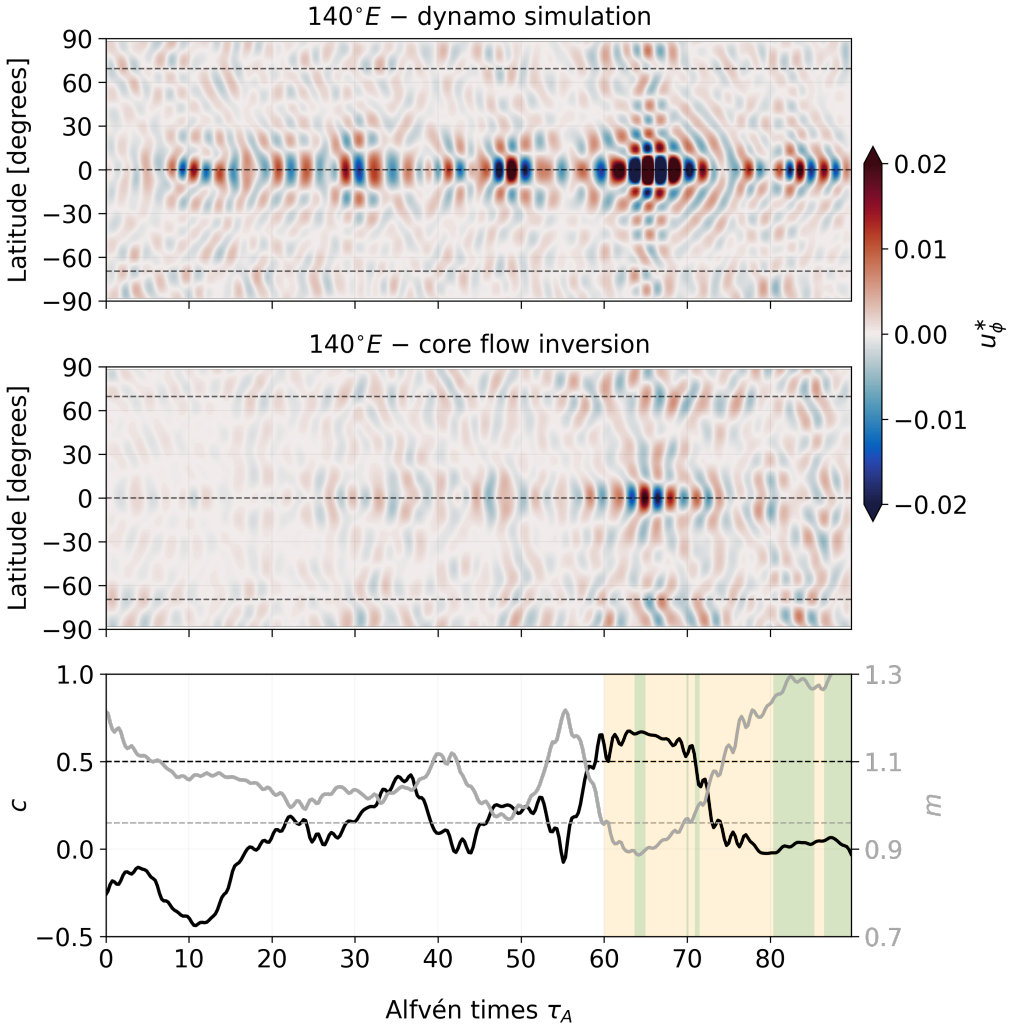

Figure 5: Time-latitude diagrams for the azimuthal flow band-pass filtered between 2 and 4.5 τ_A, at longitude $\phi_0 = 140°$E: reference dynamo flow (top) and ensemble average of the inverted flow models (middle). Bottom: correlation coefficient ($c(t)$, black) and misfit ($m(t)$, in grey). The dotted lines at $c = 0.5$ (black) and $m = 0.96$ (grey) correspond to the 5% of positive recovery threshold from the statistical test (see Section 3.1 for details). Shaded areas correspond to the times when satellite measurements are available (green) and to the era with the most numerous ground stations and the highest accuracy magnetometers (orange).

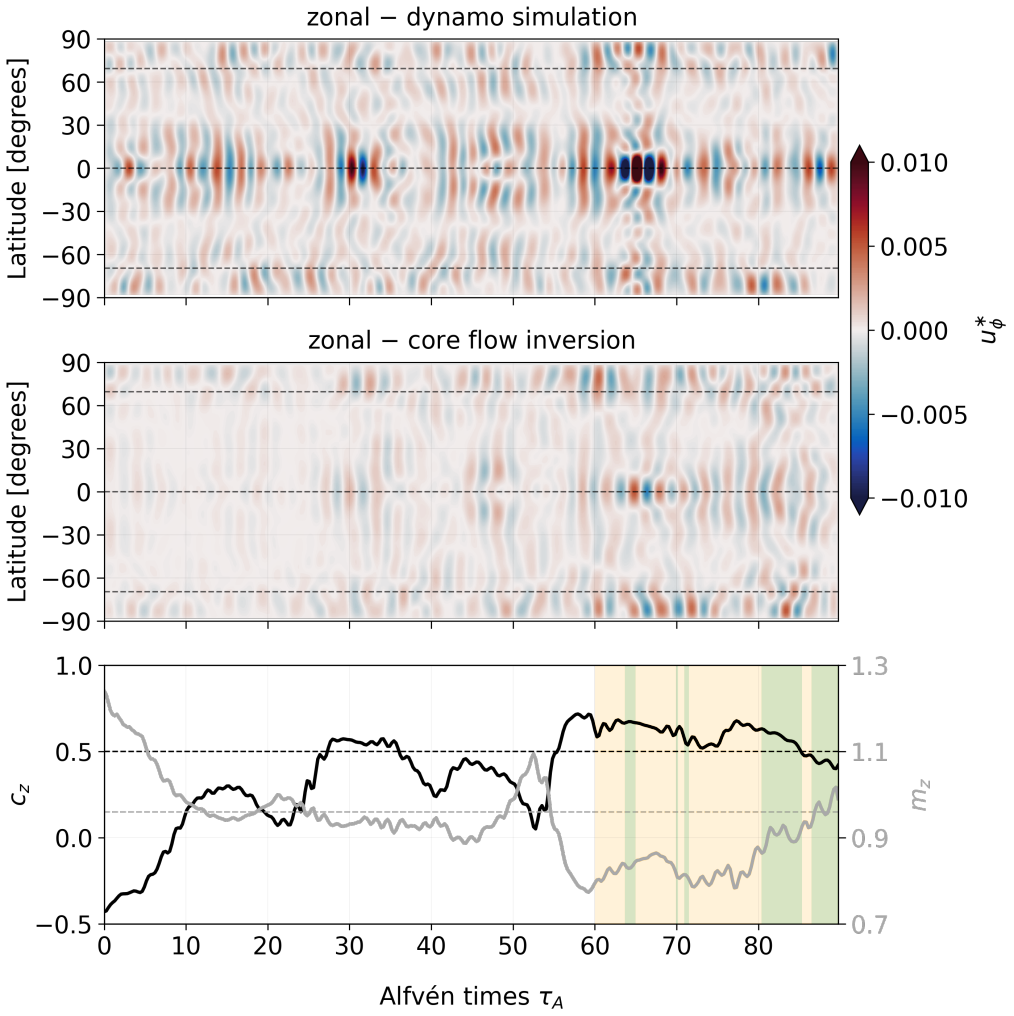

Figure 6: Same as Fig. 5, for the mean zonal flow.

The unit vectors in the cylindrical radial coordinate system are denoted $(\mathbf{1}_s, \mathbf{1}_\phi, \mathbf{1}_z)$, $\mathcal{V}$ is the Earth's core volume, $I_c = \dfrac{8\pi}{15}\rho c^5$ is the moment of inertia of the core and

$$u_\phi^0(r,\theta,t) = \frac{1}{2\pi}\int_0^{2\pi} u_\phi(r,\theta,\phi,t)\,\mathrm{d}\phi \tag{10}$$

is the zonal (axisymmetric) average of the azimuthal flow. Non-zonal motions do not contribute to the core angular momentum. The calculation of L_z requires the knowledge of the zonal velocity field throughout the entire outer core. However, under the assumption that the Coriolis force dominates the momentum balance, in a geostrophic equilibrium with the pressure gradient, zonal motions are invariant along the rotation axis ($\partial u_\phi^0/\partial z = 0$) and only depend on a single spatial variable, the cylindrical radius ($u_\phi^0 = u_\phi^0(s)$). Taking advantage of this, Jault et al. (1988) proposed to calculate the accelerations of geostrophic cylinders from the zonal toroidal part of time-dependent inverted core surface flows – represented by flow coefficients ${}^c t_n^0$ in Eq. (4). Assuming that I_c is constant, and that u_ϕ^0 is well represented by core surface motions (i.e. coefficients ${}^c t_n^0$), the rate of change of the axial angular momentum $\hat{L}_z$ for an incompressible fluid is provided by

$$\frac{\mathrm{d}\hat{L}_z}{\mathrm{d}t} = I_c\frac{\mathrm{d}\Omega}{\mathrm{d}t} + \frac{I_c}{c}\,\frac{\mathrm{d}}{\mathrm{d}t}\left({}^c t_1^0 + \frac{12}{7}{}^c t_3^0\right) . \tag{11}$$

Conservation of angular momentum for motions restricted to geostrophic flows can therefore be transformed into changes in the LOD (Jackson et al., 1993; Jault and Finlay, 2015), as

$$\delta\hat{T}(t) = \frac{T^2}{2\pi c}\frac{I_c}{I_m + I_c}\delta\left({}^c t_1^0 + \frac{12}{7}{}^c t_3^0\right) = K\delta\left({}^c t_1^0 + \frac{12}{7}{}^c t_3^0\right) , \tag{12}$$

with $T = 86\,400$ s the day length and I_m the moment of inertia of the mantle. In the considered numerical simulation, $I_m = 7.69\, I_c$, so that for flow coefficients ${}^c t_n^0$ in km/y and δT in ms, one has $K \simeq 1.24$ ms.yr/km.

4.2. LOD from (inverted) core surface flows

We first test the validity of the geostrophic assumption by calculating the perturbation to the angular momentum (in LOD units), inferred from core surface motions directly extracted from the dynamo simulation. This gives a very good prediction of the LOD in

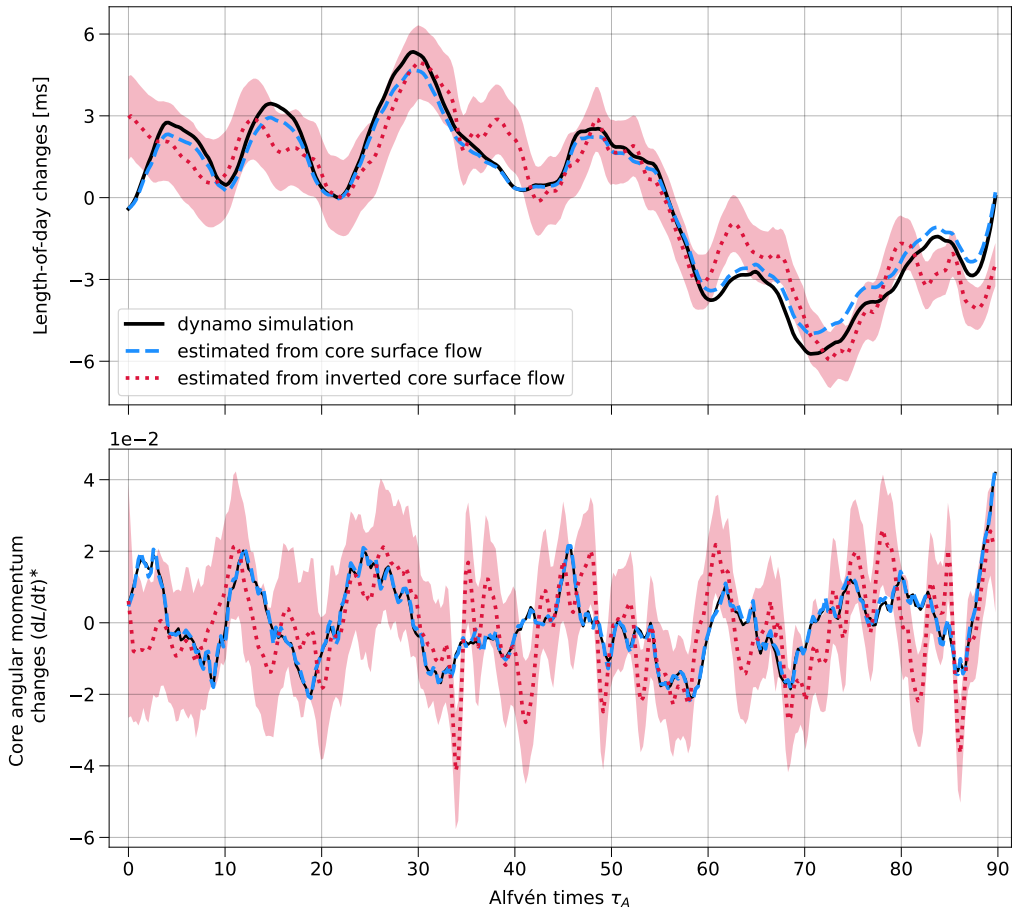

Figure 7: Time changes of the torque (bottom, sum of the gravitational and EM torques) and associated LOD changes (top) for the dynamo simulation (black), superimposed with the same quantities estimated under the geostrophic approximation (Eq. 11-12, blue). Estimates from inverted core flow: the ensemble average (red, dotted curve), and the $\pm\sigma$ spread within the ensemble (red, shaded area).

the simulation, leaving little room for a deviation between geostrophic flows and zonal flows at the core surface (Fig. 7, top). The remaining discrepancy between the actual core angular momentum and its estimate from surface flows appears in phase with the time varying angular momentum, and amounts to about 10% of the total LOD changes. Fig. 7 (bottom) shows a similar agreement, but for the torque (time derivative of the angular momentum) estimated from the zonal core surface motions – see Eq. (11). Considering the torque ($\propto \mathrm{d}LOD/\mathrm{d}t$) comes down to considering changes in the zonal motions.

Finally, we add a comparison with the LOD and torque calculated from the surface flows estimated using SV synthetic data. The LOD is rather well explained by motions deduced from geomagnetic field data, with some spurious changes though. This high-frequency noise features prominently in time series of the total torque obtained as the time derivative of the angular momentum estimated from inverted core surface motions (Fig. 7, bottom).

5. Torques acting on the mantle

5.1. Calculating the electromagnetic torque

The EM torque acting on the mantle can be estimated from geomagnetic field models and core surface flows. It results from the temporal variations of the magnetic field that emanates from the core surface and the relative motions between the core and mantle (Rochester, 1960, 1962; Roberts, 1972; Stix and Roberts, 1984). Its axial component is given by

$$\Gamma_{EM} = \mathbf{1}_z \cdot \int_{\mathcal{V}} \mathbf{r} \times (\mathbf{j} \times \mathbf{B}) \, \mathrm{d}\mathcal{V} \,, \tag{13}$$

with $\mathcal{V}$ the volume of the outer core. It can be reduced to a surface integral at the CMB,

$$\Gamma_{EM} = -\frac{c}{\mu} \int_{\mathcal{S}} B_r B_\phi \sin\theta \, \mathrm{d}\mathcal{S} \,, \tag{14}$$

with $\mathcal{S}$ the surface of the outer core.

To estimate Γ_{EM}, we follow the derivations by Roberts (1972), Stix and Roberts (1984) and Jault and Le Mouël (1991). The induction equation in the mantle is solved using a perturbation approach. At leading order, the mantle is assumed to be electrically insulating and the electrical currents vanish, $\mathbf{j}_0 = 0$. The zeroth-order magnetic field

$\mathbf{B}_0 = -\boldsymbol{\nabla} V_0$ can thus be obtained by extrapolating the magnetic field from the Earth's surface down to the CMB.

At the next order the Faraday and Ohm laws give

$$\forall r \in [c, a], \qquad \boldsymbol{\nabla} \times \frac{\mathbf{j}_1}{\sigma_m} = -\frac{\mathbf{B}_0}{\partial t} \tag{15}$$

together with a boundary condition (continuity of the tangential components of the electrical field)

$$\frac{\mathbf{1}_r \times \mathbf{j}_1}{\sigma_m} = -\mathbf{u} B_{r,0}\,, \tag{16}$$

at $r = c$. Here, we neglect the contribution of magnetic diffusion to the electrical field on the core side. We assume $|\mathbf{B}_1| \ll |\mathbf{B}_0|$ (consistent with the thin layer approximation adopted for the dynamo model). Considering instead a finite thickness of the conducting layer at the bottom of the mantle would introduce a time below which the assumption does not hold. We differentiate between "poloidal" and "toroidal" electromagnetic torques. The former is associated with time changes of the poloidal magnetic field inducing (toroidal) electrical currents in the mantle as expressed by equation (15). The latter results from toroidal magnetic fields (poloidal electrical currents) generated by core material moving with respect to the mantle in the presence of the radial magnetic field $B_{r,0}$ (see equation (16)). It is also referred to as the 'advective torque' in order to emphasize its origin (Holme, 1998). We write $(\mathbf{j}_{1,t}, \mathbf{j}_{1,p})$ the toroidal and poloidal contributions to the currents associated with the perturbation field $\mathbf{B}_1$. The poloidal and toroidal torques are therefore:

$$\left(\Gamma_{EM}\right)_p = \mathbf{1}_z \cdot \int_{\mathcal{V}} \mathbf{r} \times (\mathbf{j}_{1,t} \times \mathbf{B}_0)\, \mathrm{d}\mathcal{V}\,, \tag{17}$$

$$\left(\Gamma_{EM}\right)_t = \mathbf{1}_z \cdot \int_{\mathcal{V}} \mathbf{r} \times (\mathbf{j}_{1,p} \times \mathbf{B}_0)\, \mathrm{d}\mathcal{V}\,. \tag{18}$$

The detailed calculation of these two torques is presented in Appendix A. Reinstating the electrical currents in the expression of the electrical field on the core side of the CMB in equation (16), we would obtain an additional torque, the leakage torque, due to electrical currents leaking from the core into the mantle (Roberts, 1972; Stix and Roberts, 1984). Its calculation necessitates the knowledge of the radial derivative of $\mathbf{B}$ at the CMB. Therefore, its value cannot be estimated from geomagnetic data alone.

5.2. Electromagnetic torque estimated from the surface flows

Fig. 8(a) shows the time evolution of the EM torque, separating first between the poloidal and toroidal torques (see Appendix A), and then subdividing the latter between parts calculated from zonal and non-zonal motions. The toroidal torque dominates, amounting to about 2/3 of the total EM torque. We find that the toroidal and poloidal torques are strongly correlated. For this reason, we mainly discuss the former one in the following. The largest part of the calculated toroidal torque is associated with the solid body rotation $t_1^0(t)$. Consequently, the toroidal torque associated with non-zonal motions appears to play a secondary role.

Fig. 8(b) shows $\Gamma_{EM}(t)$ estimated from core surface magnetic fields with two different spatial resolutions. When truncating the field at the highest resolution available to us (harmonic degree 30), the calculated torque almost superimposes with the total EM torque, meaning there is little contribution from higher degrees. It also implies that there is little room for the torque, referred to above as the leakage torque, arising from the dynamo electrical currents leaking into the mantle. In the absence of other torque than the EM one, the leakage torque was assumed to cancel the torque arising from the surface motions on long time-scales as there could be no sustained acceleration of the core rotation on long periods (Stix and Roberts, 1984). The agreement between the total EM torque as obtained from the dynamo simulation and the calculated torque using a high truncation $n_b = 30$, while neglecting the leakage torque, means that the latter is negligible in the simulation. The comparison between the torques calculated with magnetic field truncation degree $n_b = 13$ and $n_b = 30$ shows that core surface magnetic fields with degrees $n \in [14, 30]$, above the actual resolution offered by geomagnetic data, bring a significant contribution to the EM torque, especially for its poloidal part. By considering the magnetic field with the actual resolution of satellite main field models ($n_b = 13$), we miss about 30% of the total torque, independently of the truncation degree of the velocity field.

Fig. 8(c) compares the EM torque calculated from the field and flow inverted from synthetic data, with the EM torque calculated from the surface flow and magnetic field of the simulation, using the same truncation degree $n_b = 13$. We find that considering the inverted field and flow (instead of the ones directly extracted from dynamo) leads to

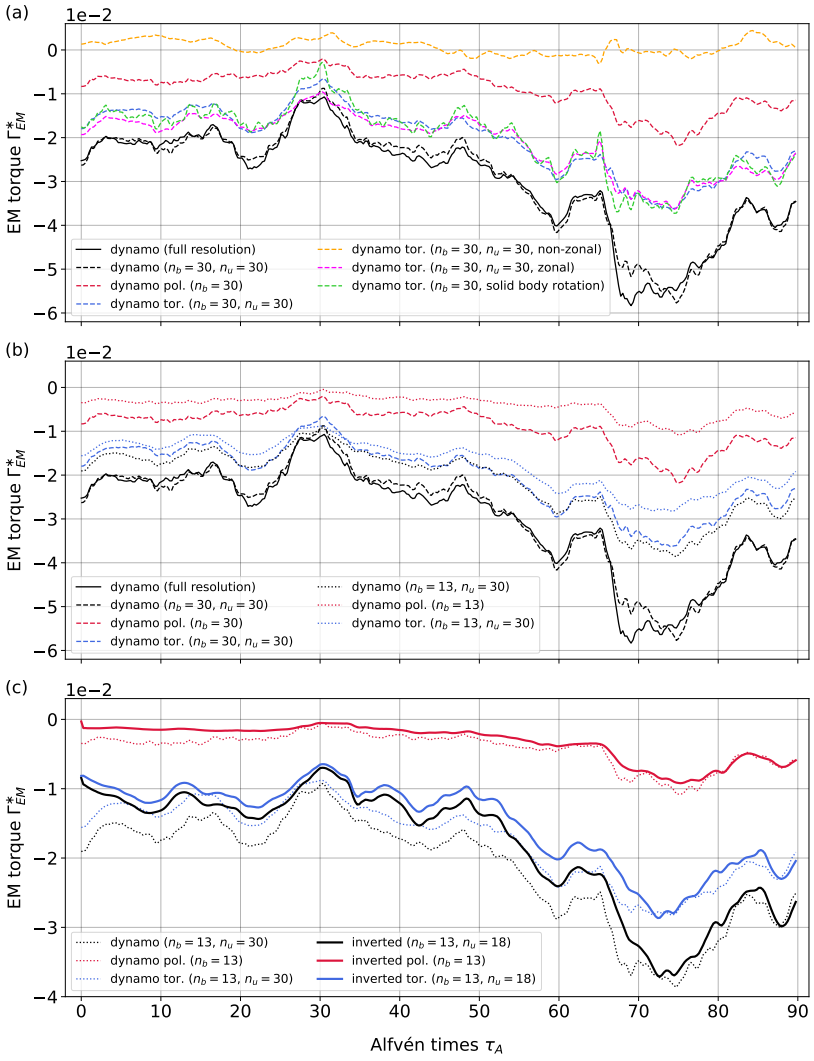

Figure 8: (a) Total EM torque on the mantle (full black curve) vs torques calculated from the core surface magnetic field and flow (dashed curves): total torque calculated with truncation degrees $n_b = 30$ and $n_u = 30$ (black), separation of the total EM torque between its poloidal (red) and toroidal (blue) parts, toroidal torque divided into parts arising from the non-zonal (orange) and zonal (pink) motions, toroidal torque arising only from the solid body rotation (green). (b) EM torque estimate as a function of the truncation degree of the magnetic field n_b: total (black), poloidal (red) and toroidal (blue) torques calculated with $n_b = 30$ (dashed) and $n_b = 13$ (dotted), with $n_u = 30$. (c) EM torque calculated with the flow ($n_u = 30$) and the magnetic field ($n_b = 13$) from the simulation (dotted curves), versus that calculated using the flow ($n_u = 18$) and the magnetic field ($n_b = 13$) inverted from synthetic data (bold lines): total (black), poloidal (red) and toroidal (blue) torques.

only slightly under-estimate the calculated torque (for a magnetic field truncated at the same degree in both cases). Both show a similar time dependence. For the most recent epochs (accurate magnetic field models), the curves almost superimpose.

On long periods, changes of $\Gamma_{EM}(t)$ seen in Fig. 8 are almost cancelled by the gravitational torque $\Gamma_G(t)$. This transpires from Fig. 7(bottom), which shows that the total torque actually evolves on shorter time-scales than Γ_{EM} alone.

6. Discussion

6.1. Recovery of interannual and decadal changes

Here, we have presented an evaluation for the reconstruction of transient core surface motions. The study is based on synthetic data from a numerical simulation of the geodynamo in which the turn-over, magnetic and inertial times are sufficiently distinct to give rise to a variety of hydromagnetic waves. This allowed us to assess our ability to recover transient motions over different time-scales. We have shown that the correctness of the inverted flows depends on a combination of the data quality and coverage, the amplitude of the flow and its geometry, as well as the considered period band. We find that

(i) Wave-like motions are better recovered when they are more intense. This favors their recovery near the equator because transient core motions are the strongest there.

(ii) Global coverage with satellite data qualify as a favorable configuration; so does a ground observatory network provided proton magnetometers are available in a number of sites, as happened after the geophysical year (1958). Note that the presence of global satellite coverage is not a sufficient condition if the flow magnitude is not high enough.

(iii) Transient motions are best recovered on longer time-scales, since for a given amplitude of the flow perturbation, the associated magnetic perturbation increases linearly with its period, thus becoming better resolved.

(iv) The quality of the recovery is also sensitive to the geometry of the reconstructed flow. Notably, zonal motions can be partly recovered before the geophysical year, despite their weak amplitude.

Our results give confidence in the QG MC waves inferred from magnetic observations using the same tools (Gillet et al., 2022a,b). We have found only a limited improvement over the period where satellite data are continuously available as compared with the earlier period covered by high quality ground observatories though. It may be the consequence of errors of representativeness in the radial induction equation (5) partly hiding the increased accuracy of the observations. Hopefully, the frequency resolution of transient motions from satellite data will improve when longer series are available.

The scaling of time with τ_A is obviously convenient when studying torsional Alfvén waves, as their period scales with τ_A. Then, the zonal motions inverted from numerical data have a magnitude of about 1 km/yr, comparable to that of zonal motions inferred from geomagnetic data (Gillet et al., 2015, 2019). This study has mainly dealt with wave-like motions with periods larger than τ_A. We have investigated two period ranges. For wave-like motions with periods respectively $[2-4.5]\tau_A$ and $[6-13.5]\tau_A$, we have estimated the outward wave velocity C to be about $U_A/10$ and $U_A/15$. We can compare these values with the geophysical estimate by Istas et al. (2023). They found the wave velocity to be about 150 km/yr ($U_A/7$) and 75 km/yr ($U_A/15$) at periods about 7 yr ($3.5\,\tau_A$) and 15 yr ($7.5\,\tau_A$). Hence, both the simulation and the geophysical model show a decrease in propagation velocity with the period.

Our study has been based on synthetic data inverted with the suite of algorithms that we currently use to analyse geophysical data. In particular the use of the COV-OBS field modeling hampers the detection of flow changes on periods shorter than $\sim 3-4$ yr. Recently, various kinds of geomagnetic data – time series from virtual observatories at satellite altitude (Hammer et al., 2021a) and time series for points at the core surface (Hammer and Finlay, 2019) – and models such as Kalmag (Baerenzung et al., 2022) have been made available that may allow us to reach shorter periods.

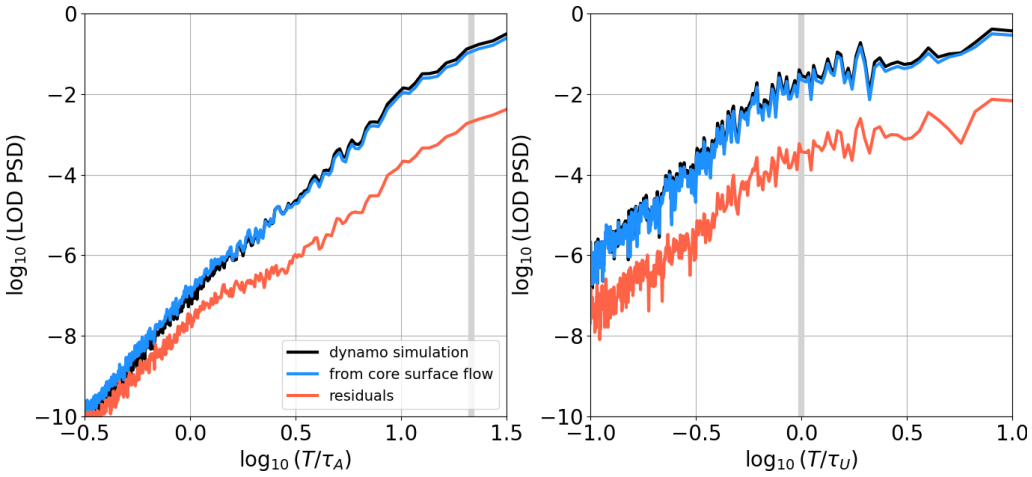

Figure 9: PSD of LOD series (in $ms^2.\tau_A$) from the *71p* dynamo (black), with time scaled based on the Alfvén time τ_A (left) and on the turn-over time τ_U (right). In blue the PSD estimated using Eq. (12), from the toroidal zonal surface flow coefficients under the geostrophic assumption. In orange the PSD for the difference of the latter two. The thick vertical grey line indicates the position of τ_U. PSD are obtained with a multi-taper method, using 20 (resp. 3) tapers for scaling time based on τ_A (resp. τ_U). For each of the tapers, a Hanning window is applied after removing the end-to-end line.

6.2. On the recovery of LOD changes

We have shown that our suite of tools allows us to convincingly recover the LOD changes of the simulation (see Fig. 7). The LOD prediction relies on the assumption that the geostrophic component is well represented by zonal core surface motions. There had never been any evaluation of this hypothesis from dynamo models before. In the simulation considered here, geostrophic motions inferred from the actual surface zonal flow $u^0_\phi(c,\theta)$ using Eq. (12) explain about 90% of the time changes of the angular momentum, validating the approach.

The validation of the hypothesis behind Eq. (12) is encouraging for the predictions conducted so far of decadal and interannual LOD changes, measured using the techniques of lunar laser ranging, very long baseline interferometry and Global Navigation Satellite Systems (Bizouard and Gambis, 2009), or lunar occultations (Gross, 2001). It also has possible implications regarding the interpretation of LOD changes on longer periods. Dumberry and Bloxham (2006) propose that millennial changes in the LOD of the order of 5 ms, as measured via eclipses (Stephenson et al., 2016), could be explained by the

core surface zonal flows being imprinted by non-geostrophic motions. Such dynamics may indeed be relatively more important towards long periods, as the geostrophic assumption is often believed to break down, because slow changes would be more affected by thermal or magnetic winds (Aubert, 2005). In this configuration, Eq. (12) is no longer valid. Dumberry and Bloxham (2006) based their scenario on the core flow models inverted from magnetic field models over the past millennia, constrained by archeomagnetic and sediment records. Our analysis of the *71p* dynamo does not fit this picture since the LOD estimate from surface motions remains right on time-scales much longer than the turnover time, i.e. some millenia (see Fig. 9, right). There are several possible explanations:

(i) The *71p* dynamo, for this specific problem, may not be representative of the Earth. The study needs confirmation from alternative dynamo simulations with a weaker gravitational torque.

(ii) The accuracy of millennial core flow changes inferred from archeomagnetic and sediment data may be poor, because of the sparser observational constraints towards ancient epochs (e.g., Licht et al., 2013; Panovska et al., 2015; Nilsson and Suttie, 2021). Furthermore, unmodelled processes at millennial time-scales are significant (see Fig. 2 in Gillet et al., 2019), and have not been considered so far in the inversion of long period flow models.

(iii) Another mechanism could be invoked, such as millenial changes in the moment of inertia of the Earth. However, the variation in ice cover and its impact on the mean sea level have been estimated to be too weak to explain ~ 5 ms millennial changes in the LOD (Hay et al., 2016).

(iv) Finally, the reconstruction of LOD changes on millennial time-scales is a difficult task as the inferred changes are obtained from the time derivative of sparse, scattered records, after interpolation (e.g., Stephenson et al., 1995; Hay et al., 2016).

The geostrophic assumption as measured by Eq. (12) appears less valid for time-scales shorter than τ_A, as shown in Fig. 9 (left). The LOD prediction, which is very good at long periods T, slightly deteriorates as T decreases below $3\tau_A$, corresponding to about 6 years. In addition, the time series inferred from inverted core surface motions show

some spurious fluctuations (see Fig. 7 bottom). This effect is partly the consequence of `pygeodyn` embedding a rather permissive forward model into a Kalman filter. It may be mitigated by using instead a smoother and/or a higher order stochastic model.

Finally, we have detected no clear resonances in LOD series from the *7i1p* dynamo, in contrast with the geophysical situation (Duan and Huang, 2020; Ding et al., 2021; Rosat and Gillet, 2023). Fig. 10 (left) shows the resonance observed at 6-yr period ($\approx 3\tau_A$) in the combined C04 series for 1962–2022 (Bizouard et al., 2019), after removing the contributions from the atmosphere and solid tides (for details, see Rosat and Gillet, 2023). We generally see no such a resonance in PSD from simulated series (Fig. 10, right). Resonance in the Earth's core may be interpreted as being due to hydro-magnetic modes of the fluid outer core (Buffett and Mound, 2005; Gillet et al., 2017). Alternatively, it may be due to gravitational oscillations of the inner core coupled with geostrophic fluid motions (Mound and Buffett, 2003, 2006). In order to test the latter hypothesis, we have to re-instate inner core inertia, which has been neglected in the dynamo simulation on which we have relied here.

6.3. On the torques acting at the CMB

The relative contribution of the poloidal torque is stronger in the simulation (on the order of 1/3) than previously estimated from geophysical data (Jault and Le Mouël, 1991; Holme, 1998). This is partly explained by the relatively large contribution of the medium scales of the magnetic field, with degrees $n \in [14, 30]$, to the poloidal torque. This contribution used to be unaccounted for. We have also shown that electrical currents generated inside the core and leaking into the mantle do not contribute much to the electromagnetic coupling. This contrasts with the mechanism (balance between diffusive and surface torques) for the westward drift of the geomagnetic field put forward by Bullard et al. (1950), and also invoked by Stix and Roberts (1984) for angular momentum changes on long time-scales. Indeed, we have been able to retrieve the EM torque neglecting these currents in the calculation of the electric field at the CMB.

The results of Pichon et al. (2016) were also at odds with the scenario of Bullard et al. (1950). They found that the long-term EM torque originating from the relative motion between the core surface and the mantle is fully balanced by the EM torque due to the relative motion between the inner and outer cores. In their simulation, the long-term

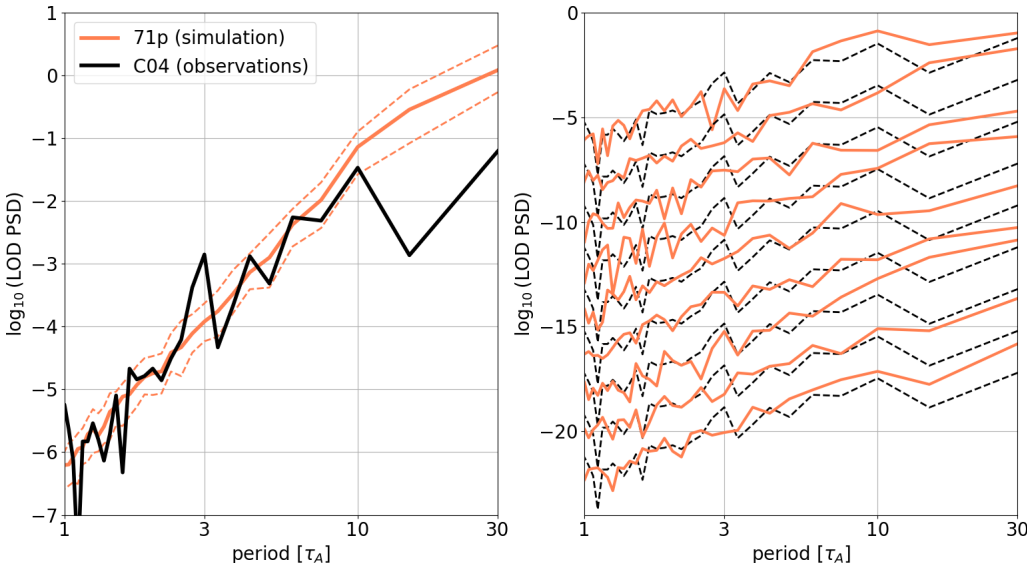

Figure 10: PSD of LOD series (in ms^2.yr). Left: in black for the geophysical series, superimposed with the median PSD for 81 series extracted from the *71p* simulation, each $30\tau_A$-long (dotted lines represent PSD for the 1st and 3rd quartiles). Right: 9 examples of PSD for $30\tau_A$-long numerical series from *71p*, superimposed with the PSD for the geophysical series (dotted black). Plots for each individual series have been shifted by two decades to avoid overlapping. PSD have been obtained after removing the end-to-end line on each of the series, and applying a Hanning window.

EM torque on the inner core is balanced by the gravitational torque. There is no room for a leakage torque. Furthermore, when the gravitational torque is zero, they found that the EM torque on the inner core vanishes also and so does the EM torque originating from the differential rotation between the core and the mantle. This applies both to the long-term parts of the EM torques and to their fluctuations. We have reproduced the results by Pichon et al. (2016) with a dynamo simulation calculated with much more extreme parameters but for only one value of the gravitational torque. In order to continue the comparison, we would need to vary the strength of the gravitational torque in the simulation. The scenario by Pichon et al. (2016) requires a gravitational torque between the inner core and the mantle. Therefore, we have to investigate whether it is specific to the suite of path-dynamos by Aubert et al. (2013, 2017), devised to produce an Earth-like westward drift.

We have also shown that the solid rotation component of the surface flow t_1^0 explains most of the toroidal EM torque, in agreement with previous geophysical studies (Jault and Le Mouël, 1991). Therefore, there are two limitations in the calculation of the EM torque. First, the small-scale part of the radial magnetic field at the CMB plays a significant role in the electromagnetic coupling. Second, we need a model of mantle conductivity, whereas magnetic field variations of magnetospheric origin unequivocally constrain electrical conductivity down to 1600 km depth only (Kuvshinov et al., 2021). Broadly speaking, these two limitations affect only the amplitude of the EM torque, not its time dependence.

Acknowledgments

We thank Julien Aubert for providing the numerical dynamo data, and for helpful discussions about their interpretation. We also thank two anonymous referees for their thorough review of our manuscript, that helped improve its quality. This work has been funded by the European Research Council (ERC) under the European Union's Horizon 2020 research and innovation programme (GRACEFUL Synergy Grant agreement No 855677) and by ESA in the framework of EO Science for Society, through contract 4000127193/19/NL/IA (Swarm + 4D Deep Earth: Core). It has also been partially supported by the French Space Agency (CNES) in the context of the *Swarm* mission of

ESA. TS, NG and DJ are part of Labex OSUG@2020 (ANR10 LABX56).

Appendix A. Calculation of the electromagnetic torque

We detail below the calculation of the poloidal and toroidal EM torques at the CMB. As for the electrical currents, we distinguish between the toroidal and poloidal electric fields, noted respectively $\mathbf{E}_{1,t}$ and $\mathbf{E}_{1,p}$).

Appendix A.1. Poloidal electromagnetic torque

Changes in the poloidal magnetic field originating from the core induce toroidal electric currents in the conducting mantle, which are given by

$$\mathbf{j}_{1,t} = \sigma_m \mathbf{E}_{1,t} = -\sigma_m \nabla \times \left(\dot{P}_0 \, r \mathbf{1}_r \right), \tag{A.1}$$

where $\dot{P}_0$ is the time derivative of the poloidal magnetic potential. According to Eq. (17), the associated electromagnetic torque can now be written as

$$\left(\Gamma_{EM}\right)_p = \int_{\mathcal{V}} \sigma_m(r) \, B_{r,0} \frac{\partial \dot{P}_0}{\partial \varphi} r^2 \, \mathrm{d}\mathcal{V}. \tag{A.2}$$

Spherical harmonic expansions of $B_{r,0}$ and P_0 can be derived from Eq. (2) using $B_{r,0} = -\partial V/\partial r$ and $\partial(rP_0)/\partial r = -V$. The above equation can then be transformed into

$$\left(\Gamma_{EM}\right)_p = -4\pi a^2 \sum_n \sum_m \alpha_n^m \left(g_n^m \dot{h}_n^m - h_n^m \dot{g}_n^m \right) \int_c^a \sigma_m(r) \left(\frac{a}{r} \right)^{2n+2} r^2 \, \mathrm{d}r \,, \tag{A.3}$$

$$\text{with } \alpha_n^m = \frac{m\,(n+1)}{n\,(2n+1)} \,.$$

In the case of the Earth, a model for the electric conductivity of the mantle $\sigma_m(r)$ would be required to evaluate this expression for the poloidal electromagnetic torque. If the conductivity is assumed uniform throughout the layer (as is the case in the *71p* dynamo), it simplifies to

$$\left(\Gamma_{EM}\right)_p = -4\pi a^5 \sigma_m \sum_n \sum_m \left(g_n^m \dot{h}_n^m - h_n^m \dot{g}_n^m \right) \frac{\alpha_n^m}{2n-1} \left(\frac{a}{c} \right)^{2n-1} \left[1 - \left(\frac{c}{c+\Delta} \right)^{2n-1} \right] \tag{A.4}$$

In the thin layer approximation $\Delta \ll c$, this expression reduces to

$$\left(\Gamma_{EM}\right)_p = 4\pi a^4 G \sum_n \sum_m \alpha_n^m \left(g_n^m \dot{h}_n^m - h_n^m \dot{g}_n^m \right) \left(\frac{a}{c} \right)^{2n} . \tag{A.5}$$

Appendix A.2. Toroidal electromagnetic torque

The toroidal electromagnetic torque arises from the rearrangement of the magnetic flux lines emanating from the core due to fluid motions (of an assumed perfectly conducting fluid) beneath the core surface. The resulting induced poloidal electric currents in the mantle are given by

$$\mathbf{j}_{1,p} = \sigma_m \mathbf{E}_{1,p} = \frac{1}{\mu} \nabla \times \nabla \times (r\mathbf{1}_r W_1) = -\sigma_m \nabla \psi_1, \tag{A.6}$$

where W_1 is the toroidal potential of the first-order magnetic field in the mantle and ψ_1 is a scalar potential. Using the vector identity $\nabla \times \nabla \times \mathbf{A} = \nabla (\nabla \cdot \mathbf{A}) - \nabla^2 \mathbf{A}$ this can be rewritten as (for a uniform lower mantle conductivity)

$$\nabla \left(\psi_1 + \eta_m \frac{\partial}{\partial r} (rW_1) \right) = \eta_m r \nabla^2 W_1 \mathbf{1}_r, \tag{A.7}$$

with $\eta_m = (\mu \sigma_m)^{-1}$. From this follows

$$\psi_1 = -\eta_m \frac{\partial}{\partial r} (rW_1) \,, \tag{A.8}$$

$$\nabla^2 W_1 = 0 \,. \tag{A.9}$$

Expanding the toroidal potential into spherical harmonics yields

$$W_1 (r, \theta, \phi) = \sum_n \sum_m \left({}^c w_n^m (r) \cos m\phi + {}^s w_n^m (r) \sin m\phi \right) P_n^m (\cos \theta) \,. \tag{A.10}$$

Knowing that the toroidal potential has to vanish at the boundary to the insulating mantle ($r = c + \Delta$), we can write

$${}^{c,s} w_n^m (r) = {}^{c,s} A_n^m \left[\left(\frac{r}{c+\Delta} \right)^n - \left(\frac{r}{c+\Delta} \right)^{-n-1} \right] . \tag{A.11}$$

To determine ${}^{c,s} w_n^m (r)$, a second boundary condition is needed. It can be obtained by determining the potential ψ_1 at the CMB. To this end, we take advantage of the continuity of the tangential component of the electric field across the CMB. By additionally assuming the core fluid to be a perfect electrical conductor, Ohm's law for a moving conductor yields at the core surface

$$\mathbf{1}_r \times \mathbf{E}_1 = \mathbf{1}_r \times (\mathbf{E}_{1,p} + \mathbf{E}_{1,t}) = \mathbf{1}_r \times (-\nabla \psi_1 + \mathbf{E}_{1,t}) = \mathbf{1}_r \times (-\mathbf{u} \times \mathbf{B}_0) = -\mathbf{u} B_{r,0} \tag{A.12}$$

By restricting (A.12) to its toroidal part it can be seen that the potential ψ_1 can be derived from the toroidal component of $\mathbf{u}B_{r,0}$:

$$\left(\mathbf{u}B_{r,0}\right)_t = -\nabla \times \left(\mathbf{1}_r \psi_1\right) = \nabla \times \left(r\mathbf{1}_r \zeta\right) , \tag{A.13}$$

with the scalar potential

$$\zeta\left(\theta,\phi\right) = \sum_n \sum_m \left({}^c\zeta_n^m \cos m\phi + {}^s\zeta_n^m \sin m\phi\right) P_n^m\left(\cos\theta\right) . \tag{A.14}$$

The boundary condition for the CMB is thus given by

$$\psi_1\left(c,\theta,\phi\right) = -c\,\zeta\left(\theta,\phi\right). \tag{A.15}$$

Together with Eq. (A.8) this expression allows the determination of ${}^{c,s}A_n^m$ in Eq. (A.11). Equation (A.10) can then be rewritten as

$$W_1\left(r,\theta,\phi\right) = \frac{c}{\eta_m} \sum_n \sum_m \frac{1}{q_n(r)} \left({}^c\zeta_n^m \cos m\phi + {}^s\zeta_n^m \sin m\phi\right) P_n^m\left(\cos\theta\right), \tag{A.16}$$

where

$$q_n(r) = \frac{\left(n+1\right)\left(\dfrac{c}{c+\Delta}\right)^n + n\left(\dfrac{c}{c+\Delta}\right)^{-n-1}}{\left(\dfrac{r}{c+\Delta}\right)^n - \left(\dfrac{r}{c+\Delta}\right)^{-n-1}} . \tag{A.17}$$

Evaluated at $r = c$ in the thin layer approximation, these coefficients simplify to

$$q_n(c) = -\frac{c}{\Delta} . \tag{A.18}$$

Noting that $\left(B_{r,1}\right)_t = 0$, writing the expression of the toroidal electromagnetic torque (Eq. 18) as a surface integral yields

$$\left(\Gamma_{EM}\right)_t = -\frac{c}{\mu} \int_{\mathcal{S}} B_{r,0} \left(B_{\phi,1}\right)_t \sin\theta \,\mathrm{d}\mathcal{S}. \tag{A.19}$$

The toroidal part of the first-order azimuthal magnetic field at the CMB can be obtained from

$$\left(B_{\phi,1}\right)_t = -\frac{\partial W_1\left(c,\theta,\phi\right)}{\partial\theta}. \tag{A.20}$$

Inserting the spherical harmonic expansions of $B_{r,0}$ and $\left(B_{\phi,1}\right)_t$ into expression (A.19) and using the recurrence relation between Ferrers normalized associated Legendre functions

$P_{n,m}$

$$\sin\theta \frac{\mathrm{d}P_{n,m}}{\mathrm{d}\theta} = \frac{(n-m+1)}{(2n+1)} P_{n+1,m} - \frac{(n+1)(m+n)}{2n+1} P_{n-1,m}, \tag{A.21}$$

allows us to write the toroidal electromagnetic torque acting on the mantle as

$$(\Gamma_{EM})_t = -4\pi c^4 \sigma_m \sum_{n=1}^{\infty} \sum_{m=0}^{n} \left(\frac{a}{c}\right)^{n+2} \left[\frac{\beta_n^m}{q_{n+1}} \left({}^c\zeta_{n+1}^m g_n^m + {}^s\zeta_{n+1}^m h_n^m \right) - \frac{\gamma_n^m}{q_{n-1}} \left({}^c\zeta_{n-1}^m g_n^m + {}^s\zeta_{n-1}^m h_n^m \right) \right] \tag{A.22}$$

with $\beta_n^m = \dfrac{(n+1)(n+2)(m+n+1)\lambda_{n+1}^m}{(2n+1)(2n+3)\lambda_n^m}$, $\gamma_n^m = \dfrac{(n+1)(n-1)(n-m)\lambda_{n-1}^m}{(2n+1)(2n-1)\lambda_n^m}$,

and where

$$\lambda_n^m = \sqrt{\frac{2(n-m)!}{(n+m)!}} \ \forall\ m \neq 0 \ \text{ and } \ \lambda_n^0 = 1 \tag{A.23}$$

are the coefficients relating the Ferrers normalized to the semi-Schmidt normalized Legendre functions $P_n^m = \lambda_n^m P_{n,m}$. In the thin layer approximation, Eq. (A.22) combined with (A.18) gives

$$(\Gamma_{EM})_t = 4\pi c^3 G \sum_{n=1}^{\infty} \sum_{m=0}^{n} \left(\frac{a}{c}\right)^{n+2} \left[\beta_n^m \left({}^c\zeta_{n+1}^m g_n^m + {}^s\zeta_{n+1}^m h_n^m \right) - \gamma_n^m \left({}^c\zeta_{n-1}^m g_n^m + {}^s\zeta_{n-1}^m h_n^m \right) \right] . \tag{A.24}$$

References

Abarca del Rio, R., Gambis, D., Salstein, D., 2000. Interannual signals in length of day and atmospheric angular momentum, in: Annales Geophysicae, Springer. pp. 347–364.

Amit, H., Olson, P., Christensen, U., 2007. Tests of core flow imaging methods with numerical dynamos. Geophys. J. Int. 168, 27–39.

Aubert, J., 2005. Steady zonal flows in spherical shell dynamos. J. Fluid Mech. 542, 53–67.

Aubert, J., 2013. Flow throughout the Earth's core inverted from geomagnetic observations and numerical dynamo models. Geophys. J. Int. 192, 537–556.

Aubert, J., 2014. Earth's core internal dynamics 1840–2010 imaged by inverse geodynamo modelling. Geophys. J. Int. 197, 1321–1334.

Aubert, J., 2018. Geomagnetic acceleration and rapid hydromagnetic wave dynamics in advanced numerical simulations of the geodynamo. Geophys. J. Int. 214, 531–547.

Aubert, J., 2020. Recent geomagnetic variations and the force balance in earth's core. Geophys. J. Int. 221, 378–393.

819 Aubert, J., Finlay, C.C., 2019. Geomagnetic jerks and rapid hydromagnetic waves focusing at Earth's
820 core surface. Nature Geoscience 12, 393–398.
821 Aubert, J., Finlay, C.C., Fournier, A., 2013. Bottom-up control of geomagnetic secular variation by the
822 Earth's inner core. Nature 502, 219–223. doi:10.1038/nature12574.
823 Aubert, J., Gastine, T., Fournier, A., 2017. Spherical convective dynamos in the rapidly rotating
824 asymptotic regime. J. Fluid Mech. 813, 558–593.
825 Aubert, J., Gillet, N., 2021. The interplay of fast waves and slow convection in geodynamo simulations
826 nearing Earth's core conditions. Geophys. J. Int. 225, 1854–1873.
827 Aubert, J., Labrosse, S., Poitou, C., 2009. Modelling the palaeo-evolution of the geodynamo. Geophys.
828 J. Int. 179, 1414–1428.
829 Aubert, J., Livermore, P.W., Finlay, C.C., Fournier, A., Gillet, N., 2022. A taxonomy of simulated
830 geomagnetic jerks. Geophys. J. Int. 231, 650–672.
831 Backus, G.E., 1968. Kinematics of geomagnetic secular variation in a perfectly conducting core. Phil.
832 Trans. R. Soc. A 263, 239–266.
833 Baerenzung, J., Holschneider, M., Saynisch-Wagner, J., Thomas, M., 2022. Kalmag: a high spatio
834 temporal model of the geomagnetic field. Earth, Planets and Space 74, 139.
835 Baerenzung, J., Holschneider, M., Wicht, J., Sanchez, S., Lesur, V., 2018. Modeling and predicting the
836 short term evolution of the geomagnetic field. J. Geophys. Res.: Solid Earth 123, 4539–4560.
837 Barrois, O., Gillet, N., Aubert, J., 2017. Contributions to the geomagnetic secular variation from a
838 reanalysis of core surface dynamics. Geophys. J. Int. 211, 50–68.
839 Bizouard, C., Gambis, D., 2009. The combined solution C04 for Earth Orientation Parameters consistent
840 with International Terrestrial Reference Frame 2005, in: Geodetic reference frames. Springer, pp. 265–
841 270.
842 Bizouard, C., Lambert, S., Gattano, C., Becker, O., Richard, J.Y., 2019. The IERS EOP 14C04 solution
843 for Earth orientation parameters consistent with ITRF 2014. Journal of Geodesy 93, 621–633.
844 Braginsky, S.I., 1967. Magnetic waves in the earth's core. Geomagn. Aeron. 7, 851–859.
845 Braginsky, S.I., 1970. Torsional magnetohydrodynamic vibrations in the earth's core and variations in
846 day length. Geomagn. Aeron. 10, 3–12.
847 Buffett, B., Mathews, P., Herring, T., 2002. Modeling of nutation and precession: effects of electromag-
848 netic coupling. J. Geophys. Res.: Solid Earth 107, ETG–5.
849 Buffett, B., Mound, J., 2005. A Green's function for the excitation of torsional oscillations in the earth's
850 core. J. Geophys. Res.: Solid Earth 110.
851 Buffett, B.A., 1996. Gravitational oscillations in the length of day. Geophys. Res. Lett. 23, 2279–2282.
852 Buffett, B.A., Mound, J., Jackson, A., 2009. Inversion of torsional oscillations for the structure and
853 dynamics of earth's core. Geophys. J. Int. 177, 878–890.
854 Bullard, E.C., Freedman, C., Gellman, H., Nixon, J., 1950. The westward drift of the Earth's magnetic
855 field. Phil. Trans. R. Soc. A 243, 67–92.
856 Christensen, U.R., Aubert, J., Hulot, G., 2010. Conditions for Earth-like geodynamo models. Earth
857 Planet. Sci. Lett. 296, 487–496.

Chulliat, A., Maus, S., 2014. Geomagnetic secular acceleration, jerks, and a localized standing wave at the core surface from 2000 to 2010. J. Geophys. Res.: Solid Earth 119, 1531–1543.

Cox, G., Livermore, P., Mound, J., 2016. The observational signature of modelled torsional waves and comparison to geomagnetic jerks. Phys. Earth Planet. Int. 255, 50–65.

Ding, H., An, Y., Shen, W., 2021. New evidence for the fluctuation characteristics of intradecadal periodic signals in length-of-day variation. J. Geophys. Res.: Solid Earth 126, e2020JB020990.

Dormy, E., 2016. Strong field spherical dynamos. J. Fluid Mech. 789, 500–513.

Duan, P., Huang, C., 2020. Intradecadal variations in length of day and their correspondence with geomagnetic jerks. Nature communications 11, 1–8.

Dumberry, M., Bloxham, J., 2006. Azimuthal flows in the earth's core and changes in length of day at millennial timescales. Geophys. J. Int. 165, 32–46.

Evensen, G., 2003. The ensemble Kalman filter: Theoretical formulation and practical implementation. Ocean Dyn. 53, 343–367.

Finlay, C., Lesur, V., Thébault, E., Vervelidou, F., Morschhauser, A., Shore, R., 2017. Challenges handling magnetospheric and ionospheric signals in internal geomagnetic field modelling. Space Sci Rev 206, 157–189.

Finlay, C.C., 2008. Course 8. Waves in the presence of magnetic fields, rotation and convection, in: P., C., Cugliandolo, L. (Eds.), Dynamos. Elsevier. volume 88 of *Les Houches*, pp. 403–450.

Finlay, C.C., Dumberry, M., Chulliat, A., Pais, M.A., 2010. Short timescale core dynamics: theory and observations. Space Sci Rev 155, 177–218.

Finlay, C.C., Olsen, N., Kotsiaros, S., Gillet, N., Toeffner-Clausen, L., 2016. Recent geomagnetic secular variation from swarm and ground observatories as estimated in the chaos-6 geomagnetic field model. Earth Planets Space 68, 1–18.

Fournier, A., Aubert, J., Thébault, E., 2011. Inference on core surface flow from observations and 3-D dynamo modelling. Geophys. J. Int. 186, 118–136.

Friedman, J., Hastie, T., Tibshirani, R., 2007. Sparse inverse covariance estimation with the graphical lasso. Biostatistics 9, 432–441.

Garland, G.D., 1979. The contributions of Carl Friedrich Gauss to geomagnetism. Historia Mathematica 6, 5–29.

Gerick, F., Jault, D., Noir, J., 2021. Fast Quasi-Geostrophic Magneto-Coriolis Modes in the Earth's Core. Geophys. Res. Lett. 48, e2020GL090803.

Gillet, N., Gerick, F., Angappan, R., Jault, D., 2022a. A dynamical prospective on interannual geomagnetic field changes. Surveys in Geophysics 43, 71–105.

Gillet, N., Gerick, F., Jault, D., Schwaiger, T., Aubert, J., Istas, M., 2022b. Satellite magnetic data reveal interannual waves in Earth's core. PNAS 119, e2115258119.

Gillet, N., Huder, L., Aubert, J., 2019. A reduced stochastic model of core surface dynamics based on geodynamo simulations. Geophys. J. Int. 219, 522–539.

Gillet, N., Jault, D., Canet, E., 2017. Excitation of travelling torsional normal modes in an earth's core model. Geophys. J. Int. 210, 1503–1516.

Gillet, N., Jault, D., Canet, E., Fournier, A., 2010. Fast torsional waves and strong magnetic field within the Earth's core. Nature 465, 74–77.

Gillet, N., Jault, D., Finlay, C.C., 2015. Planetary gyre, time-dependent eddies, torsional waves, and equatorial jets at the Earth's core surface. J. Geophys. Res.: Solid Earth 120, 3991–4013.

Gillet, N., Jault, D., Finlay, C.C., Olsen, N., 2013. Stochastic modeling of the Earth's magnetic field: Inversion for covariances over the observatory era. Geochemistry, Geophysics, Geosystems 14, 766–786.

Greenspan, H.P., 1968. The theory of rotating fluids. Technical Report. Massachusetts Inst of Tech Cambridge Dept of Mathematics.

Gross, R.S., 2001. A combined length-of-day series spanning 1832–1997: Lunar97. Phys. Earth Planet. Int. 123, 65–76.

Hammer, M.D., Cox, G.A., Brown, W.J., Beggan, C.D., Finlay, C.C., 2021a. Geomagnetic virtual observatories: monitoring geomagnetic secular variation with the swarm satellites. Earth, Planets and Space 73, 54.

Hammer, M.D., Finlay, C.C., 2019. Local averages of the core–mantle boundary magnetic field from satellite observations. Geophys. J. Int. 216, 1901–1918.

Hammer, M.D., Finlay, C.C., Olsen, N., 2021b. Applications for CryoSat-2 satellite magnetic data in studies of earth's core field variations. Earth, Planets and Space 73, 73.

Hay, C., Mitrovica, J.X., Morrow, E., Kopp, R.E., Huybers, P., Alley, R.B., 2016. Earth rotation changes since- 500 ce driven by ice mass variations. Earth Planet. Sci. Lett. 448, 115–121.

Hide, R., 1966. Free hydromagnetic oscillations of the earth's core and the theory of the geomagnetic secular variation. Phil. Trans. R. Soc. A 259, 615–647.

Holme, R., 1998. Electromagnetic core-mantle coupling – I Explaining decadal changes in the length of day. Geophys. J. Int. 132, 167–180.

Holme, R., 2015. Large-Scale Flow in the Core, in: Schubert, G. (Ed.), Treatise on Geophysics (Second Edition). Elsevier, Oxford. volume 8. chapter 8.04, pp. 91–113.

Huder, L., Gillet, N., Finlay, C.C., Hammer, M.D., Tchoungui, H., 2020. COV-OBS.x2: 180 years of geomagnetic field evolution from ground-based and satellite observations. Earth, Planets and Space 72, 160.

Huder, L., Gillet, N., Thollard, F., 2019. pygeodyn 1.1. 0: a python package for geomagnetic data assimilation. Geosci. Model Dev. 12, 3795–3803.

Istas, M., Gillet, N., Finlay, C., Hammer, M., Huder, L., 2023. Transient core surface dynamics from ground and satellite geomagnetic data. Geophys. J. Int. 233, 1890–1915.

Jackson, A., Bloxham, J., Gubbins, D., 1993. Time-dependent flow at the core surface and conservation of angular momentum in the coupled core-mantle system, in: Le Mouël, J.-L. and Smylie, D. E. and Herring, T. (Ed.), Dynamics of Earth's deep interior and Earth rotation Geophysical Monograph 72 IUGG Volume 12. AGU, Washington. chapter 11, pp. 97–108.

Jackson, A., Jonkers, A.R., Walker, M.R., 2000. Four centuries of geomagnetic secular variation from historical records. Phil. Trans. R. Soc. London. Series A: Mathematical, Physical and Engineering

936 Sciences 358, 957–990.
937 Jault, D., 2003. Electromagnetic and topographic coupling, and lod variations, in: C., J., Soward, A.,
938 Zhang, K. (Eds.), Earth's core and lower mantle. CRC Press, pp. 85–107.
939 Jault, D., 2015. Illuminating the electrical conductivity of the lowermost mantle from below. Geophys.
940 J. Int. 202, 482–496.
941 Jault, D., Finlay, C., 2015. Waves in the core and mechanical core–mantle interactions, in: Schubert, G.
942 (Ed.), Treatise on Geophysics (Second Edition). Elsevier. volume 8. chapter 8.09, pp. 225–244.
943 Jault, D., Gire, C., Le Mouël, J.L., 1988. Westward drift, core motions and exchanges of angular
944 momentum between core and mantle. Nature 333, 353–356.
945 Jault, D., Le Mouël, J., 1991. Exchange of angular momentum between the core and the mantle. J.
946 Geomag. Geoelectr. 43, 111–129.
947 Jonkers, A.R., Jackson, A., Murray, A., 2003. Four centuries of geomagnetic data from historical records.
948 Reviews of Geophysics 41.
949 Kloss, C., Finlay, C.C., 2019. Time-dependent low-latitude core flow and geomagnetic field acceleration
950 pulses. Geophys. J. Int. 217, 140–168.
951 Koot, L., Dumberry, M., Rivoldini, A., De Viron, O., Dehant, V., 2010. Constraints on the coupling at
952 the core–mantle and inner core boundaries inferred from nutation observations. Geophys. J. Int. 182,
953 1279–1294.
954 Kuvshinov, A., Grayver, A., Tøffner-Clausen, T., Olsen, N., 2021. Probing 3-D electrical conductivity of
955 the mantle using 6 years of Swarm, CryoSat-2 and observatory magnetic data and exploiting matrix
956 Q-responses approach. Earth, Planets and Space 73.
957 Lesur, V., Gillet, N., Hammer, M.D., Mandea, M., 2022. Rapid variations of earth's core magnetic field.
958 Surveys in Geophysics 43, 41–69.
959 Lesur, V., Wardinski, I., Baerenzung, J., Holschneider, M., 2018. On the frequency spectra of the core
960 magnetic field gauss coefficients. Phys. Earth Planet. Int. 276, 145–158.
961 Licht, A., Hulot, G., Gallet, Y., Thébault, E., 2013. Ensembles of low degree archeomagnetic field models
962 for the past three millennia. Phys. Earth Planet. Int. 224, 38–67.
963 Malkus, W.V.R., 1967. Hydromagnetic planetary waves. J. Fluid Mech. 28, 793–802.
964 Mandea, M., Holme, R., Pais, A., Pinheiro, K., Jackson, A., Verbanac, G., 2010. Geomagnetic jerks:
965 rapid core field variations and core dynamics. Space Sci Rev 155, 147–175.
966 Mandea, M., Olsen, N., 2006. A new approach to directly determine the secular variation from magnetic
967 satellite observations. Geophys. Res. Lett. 33.
968 Matzka, J., Chulliat, A., Mandea, M., Finlay, C.C., Qamili, E., 2010. Geomagnetic observations for
969 main field studies: from ground to space. Space Science Reviews 155, 29–64.
970 Mound, J., Buffett, B., 2003. Interannual oscillations in length of day: Implications for the structure of
971 the mantle and core. J. Geophys. Res.: Solid Earth 108.
972 Mound, J., Buffett, B., 2005. Mechanisms of core-mantle angular momentum exchange and the observed
973 spectral properties of torsional oscillations. J. Geophys. Res.: Solid Earth 110.
974 Mound, J.E., Buffett, B.A., 2006. Detection of a gravitational oscillation in length-of-day. Earth Planet.

975 Sci. Lett. 243, 383–389.
976 Nilsson, A., Suttie, N., 2021. Probabilistic approach to geomagnetic field modelling of data with age
977 uncertainties and post-depositional magnetisations. Phys. Earth Planet. Inter. 317, 106737.
978 Panovska, S., Korte, M., Finlay, C., Constable, C., 2015. Limitations in paleomagnetic data and mod-
979 elling techniques and their impact on holocene geomagnetic field models. Geophys. J. Int. 202, 402–418.
980 Pichon, G., Aubert, J., Fournier, A., 2016. Coupled dynamics of earth's geomagnetic westward drift and
981 inner core super-rotation. Earth Planet. Sci. Lett. 437, 114–126.
982 Pick, L., Korte, M., Thomas, Y., Krivova, N., Wu, C.J., 2019. Evolution of large-scale magnetic fields
983 from near-earth space during the last 11 solar cycles. J. Geophys. Res.: Space Physics 124, 2527–2540.
984 Pozzo, M., Davies, C., Gubbins, D., Alfe, D., 2012. Thermal and electrical conductivity of iron at Earth's
985 core conditions. Nature 485, 355–358.
986 Rau, S., Christensen, U., Jackson, A., Wicht, J., 2000. Core flow inversion tested with numerical dynamo
987 models. Geophys. J. Int. 141, 485–497.
988 Roberts, P.H., 1972. Electromagnetic core-mantle coupling. J. Geomag. Geoelectr. 24, 231–259.
989 Roberts, P.H., Aurnou, J.M., 2012. On the theory of core-mantle coupling. Geophys. Astrophys. Fluid
990 Dyn. 106, 157–230.
991 Roberts, P.H., Scott, S., 1965. On analysis of the Secular Variation 1. A hydrodynamic constraint:
992 Theory. J. Geomag. Geoelectr. 17, 137–151.
993 Rochester, M.G., 1960. Geomagnetic westward drift and irregularities in the Earth's rotation. Phil.
994 Trans. R. Soc. A 252, 531–555.
995 Rochester, M.G., 1962. Geomagnetic core-mantle coupling. J. Geophys. Res. 67, 4833–4836.
996 Rosat, S., Gillet, N., 2023. Intradecadal variations in length of day: Coherence with models of the earth's
997 core dynamics. Phys. Earth Planet. Inter. , 107053.
998 Sanchez, S., Wicht, J., Bärenzung, J., Holschneider, M., 2019. Sequential assimilation of geomagnetic
999 observations: perspectives for the reconstruction and prediction of core dynamics. Geophys. J. Int.
1000 217, 1434–1450.
1001 Schaeffer, N., Jault, D., 2016. Electrical conductivity of the lowermost mantle explains absorption of
1002 core torsional waves at the equator. Geophys. Res. Lett. 43, 4922–4928.
1003 Schaeffer, N., Jault, D., Nataf, H.C., Fournier, A., 2017. Turbulent geodynamo simulations: a leap
1004 towards Earth's core. Geophys. J. Int. 211, 1–29.
1005 Schwaiger, T., Gastine, T., Aubert, J., 2019. Force balance in numerical geodynamo simulations: a
1006 systematic study. Geophys. J. Int. 219, S101–S114.
1007 Stephenson, F., Morrison, L., Hohenkerk, C., 2016. Measurement of the Earth's rotation: 720 BC to
1008 AD 2015. Proc. R. Soc. A 472, 20160404.
1009 Stephenson, F.R., Morrison, L.V., Smith, F., 1995. Long-term fluctuations in the Earth's rotation: 700
1010 BC to AD 1990. Phil. Trans. R. Soc. London. Series A 351, 165–202.
1011 Stix, M., Roberts, P., 1984. Time-dependent electromagnetic core-mantle coupling. Phys. Earth Planet.
1012 Int. 36, 49–60.
1013 Teed, R.J., Jones, C.A., Tobias, S.M., 2014. The dynamics and excitation of torsional waves in geody-

namo simulations. Geophys. J. Int. 196, 724–735.

Wicht, J., Christensen, U.R., 2010. Torsional oscillations in dynamo simulations. Geophys. J. Int. 181, 1367–1380.

de Wijs, G.A., Kresse, G., Vočadlo, L., Dobson, D., Alfe, D., Gillan, M.J., Price, G.D., 1998. The viscosity of liquid iron at the physical conditions of the Earth's core. Nature 392, 805–807.

Zatman, S., Bloxham, J., 1997. Torsional oscillations and the magnetic field within the Earth's core. Nature 388, 760–763.

Zatman, S., Bloxham, J., 1999. On the dynamical implications of models of Bs in the Earth's core. Geophys. J. Int. 138, 679–686.